Butyrate endows extraocular muscle stem cell-like transcriptomic patterns that ameliorate satellite cell depletion and denervation to slow ALS progression

Ang Li[1*], Jianxun Yi[1], Xuejun Li[1], Li Dong[1], Lyle W Ostrow[2], Jianjie Ma[3], Jingsong Zhou[1*]

[1] Department of Kinesiology, College of Nursing and Health Innovation, University of Texas at Arlington, TX, 76019, USA

[2] Department of Neurology, Lewis Katz School of Medicine at Temple University, Philadelphia, PA 19122, USA

[3] Department of Surgery, University of Virginia, Charlottesville, VA, 22903, USA

* Corresponding author

Abstract

Amyotrophic lateral sclerosis (ALS) is a fatal neuromuscular disease that affects all voluntary muscles in the body, leading to paralysis and respiratory failure, while the extraocular muscles (EOMs) are largely spared even at the end-stage of ALS. Through whole-mount muscle imaging, we detected severe denervation along with depletion of Pax7$^+$ satellite cells (SCs) peri-neuromuscular junction (NMJ) in hindlimb and diaphragm muscles of end-stage SOD1G93A mice (a familial ALS mouse model), but not in EOMs. Upon isolating SCs from different muscles using fluorescence activated cell sorting (FACS), the FACS profiles of hindlimb and diaphragm SCs of G93A mice exhibited activation and depletion phenotypes but not in wildtype controls. Importantly, both wildtype and G93A EOM SCs exhibited spontaneous activation behavior without significant differences in abundance. Examination of Pax7$^+$ and Ki67$^+$ cell ratios and RNA-Seq of SCs cultured in growth and differentiation medium revealed that EOM SCs maintained renewability and stemness better than diaphragm and hindlimb counterparts, especially in differentiation-favoring environments. Comparative functional annotation analyses indicate enrichment of axon guidance molecules, such as *Cxcl12*, in cultured EOM SCs. In neuromuscular coculture experiments, overexpressing *Cxcl12* in G93A hindlimb SC-derived myotubes enhanced motor neuron axon extension and improved innervation, partially replicating the multi-innervation property of EOM SC-derived myotubes. The unique SC homeostasis regulation and the production of axon guidance molecules including *Cxcl12* may explain the ALS resistant nature of EOMs. Intriguingly, feeding G93A mice with sodium butyrate extended the life span of G93A mice, alleviated NMJ denervation and SCs depletion. Butyrate treatment promoted renewability and stemness of cultured G93A hindlimb and diaphragm SCs, as well as *Cxcl12* expression. Thus, butyrate-induced EOM SC-like transcriptomic patterns may contribute to its beneficiary effects observed in G93A mice.

Key words: amyotrophic lateral sclerosis, satellite cell, neuromuscular junction, chemokine.

Abbreviations: acetylcholine receptor (AChR); amyotrophic lateral sclerosis (ALS); extensor digitorum longus (EDL); extraocular muscle (EOM); flexor digitorum brevis (FDB); hindlimb (HL); motor neuron (MN); neurobasal plus medium (NBPM); neuromuscular junction (NMJ); rat spinal motor neurons (RSMNs); tibialis anterior (TA); Sodium butyrate (NaBu).

Introduction

Amyotrophic lateral sclerosis (ALS) is a devastating disease characterized by degeneration of motor neurons and skeletal muscle wasting, which commonly results in respiratory failure and death in 3–5 years after diagnosis [1,2]. The end-stage patients or those lived longer than five years mostly rely on the eyeball movement mediated by extraocular muscles (EOMs) as a way of communication [2]. Different from motor neurons (MNs) controlling limb muscles, EOM MNs innervate fewer myofibers while individual myofiber can have multiple neuromuscular junctions (NMJs) [3,4]. The integrities of NMJs in EOMs from ALS donors and mice models are well preserved even at the end stage of the disease, whereas NMJs in limb muscles already start to loss connection with axons even before the onset of symptoms [2,5-7].

The initial studies about why EOMs are selectively spared in ALS focused on MNs themselves [8]. The MNs innervating EOMs were found to express markedly higher levels of Ca^{2+} binding protein calbindin-D28k and parvalbumin than MNs lost early in ALS, which can result in differential cytosolic Ca^{2+} homeostasis in response to extracellular stimuli [8-10]. In the recent two decades, studies of microenvironment components local to MN cell bodies and NMJs have accelerated as more evidence supporting non-cell-autonomous hypothesis of MN degeneration in ALS started to emerge. For example, astrocytes carrying mutations in SOD1, C9orf72 and astrocytes derived from sporadic ALS patients were reported to be toxic to MNs under both *in vitro* and *in vivo* conditions [11-16]. Muscle-restricted expression of familial ALS patient mutations ($SOD1^{G37R}$, $SOD1^{G93A}$) was sufficient to induce MN distal axonopathy and apoptosis [17]. In $SOD1^{G93A}$ mice, the detachment of motor neuron axons and myofibers precedes the detection of motor neuron death in the spinal cord, a phenomenon also reported in ALS patients who died of other reasons early in the course of ALS [18]. In contrast, muscle-specific expression of an Igf-1 isoform improved neuromuscular junction integrity and motor neuronal survival in mice overexpressing $SOD1^{G93A}$ (G93A for short) in all tissue, delaying the onset and progression of the disease [19].

Previously, efforts have been made to identify neuroprotective molecules derived from EOM myofibers, which may explain the well-preserved NMJs at the end stage of ALS [20,21]. Surprisingly, in either $SOD1^{G93A}$ mice or wild type (WT) controls, the expression of classical neurotrophic factors such as BDNF, GDNF, NT3 and NT4 in EOM myofibers were found to be either lower or comparable to limb muscles [20,21]. Thus, aside from doing more systematic screening in myofibers, it is also worthwhile to look for clues in other microenvironmental components of NMJs, such as satellite cells (SCs).

The association between SCs and NMJ integrity has been explored in the context of denervation (by surgery) and aging in animal models previously [22,23]. Denervation induced muscle atrophy, muscle type transition, fibrosis and declines in muscle force were all exacerbated in SC depleted transgenic mice compared to control littermates. SC depletion also led to deficits in skeletal muscle reinnervation, reductions in post-synaptic morphology and loss of post-synaptic myonuclei [22]. Using a transgenic mice expressing GFP in the progeny of activated SCs, the authors observed increased contributions of SCs to the myofiber in the vicinity of NMJs after denervation [22]. The group also investigated whether aging-related NMJ degeneration is associated with decreased abundance of SCs [23]. They detected accelerated NMJ deterioration in SC depleted mice. In contrast, the preservation of SC pool by overexpressing Spry1 resulted in attenuation of aging-related NMJ degeneration and improved muscle performance in aged mice [23]. The above two studies laid a foundation of the active role of SCs in the maintenance and regeneration of NMJs. Since SCs from EOMs have been reported to exhibit superior expansion and renewability than their limb counterparts *in vitro* and *in vivo* [24], We are prompted to conduct transcriptomic profiling of EOM SCs to look for candidates that help preserve NMJ integrity under ALS.

Previous studies have shown the epigenetic regulation of SC transcriptome by histone deacetylase (HDAC) inhibitors, such as sodium butyrate (NaBu) [25], could modulate the myogenesis process both *in vitro* and *in vivo* [26-29]. Interestingly, our team recently discovered that feeding G93A mice with NaBu (2% in water) significantly prolonged the life span (~38 days) and ameliorated mitochondrial dysfunction in skeletal muscle and cultured NSC34 motor neurons [30-33]. It is intriguing to examine whether the beneficiary effect of NaBu is linked with SC behavior changes and whether NaBu treatment produced any epigenetic modulations similar to that of EOM SCs.

In this study, we first conducted whole-mount imaging analysis of NMJ integrity and peri-NMJ SC abundance in hindlimb (HL), diaphragm and extraocular muscles from end-stage G93A mice and age-matched wildtype (WT) controls. Except for EOM, all other types of muscles exhibited different degrees of NMJ denervation and SC depletion in G93A mice compared to WT controls. Meanwhile, NaBu fed G93A mice exhibited significant amelioration of NMJ denervation and SC depletion in HL and diaphragm muscles. The imaging data is also supported by qRT-PCR of whole-muscle RNAs for denervation markers like *Scn5a*.

Next, we isolated SCs from HL, diaphragm and extraocular muscles from end-stage G93A mice and age-matched WT controls using fluorescence-activated cell sorting (FACS). In the FACS profile, HL and diaphragm SCs derived from end stage G93A mice were less abundant than those from WT controls and exhibited more heterogenous expression of SC marker Vcam1. Surprisingly, EOM SCs exhibited heterogenous expression of Vcam1 regardless of disease state, implying they are physiologically a mixed population. RNA-Seq, qRT-PCR and immunofluorescence analysis revealed that EOM SCs have higher renewability and maintain stemness better than diaphragm and hindlimb counterparts, especially after the induction of differentiation. More intriguingly, functional annotation analysis denoted more enriched expression of axon guidance molecules, such as the chemokine *Cxcl12*, in EOM SCs cultured either in growth or differentiation medium.

Consistent with this expression pattern, EOM SC-derived myotubes, even those of G93A origin, notably enhanced axon extension and innervation in coculture experiments with rat spinal motor neurons compared to those HL SC-derived myotubes of either G93A or WT origin. These features were partially replicated by overexpressing *Cxcl12* using adeno-associated viral vector (AAV8) in G93A HL SC-derived myotubes.

More than a coincidence, applying NaBu (0.5 mM) to the culture medium also promoted the renewability and stemness of G93A HL and diaphragm SCs as shown by RNA-Seq, qRT-PCR and immunofluorescence analysis. Axon guidance molecules like *Cxcl12* were also notably induced by NaBu treatment. Thus, NaBu-induced EOM SC-like transcriptomic pattern could be a crucial contributor to its therapeutic effect against ALS progression.

Results

Comparing NMJ integrity and peri-NMJ satellite cell abundance in different muscles from wildtype controls and G93A mice with or without butyrate feeding

We initiated the project by a systematic investigation of NMJ integrity and peri-NMJ satellite cell abundance by whole-mount imaging extensor digitorum longus (EDL), soleus, diaphragm and extraocular muscles from G93A mice with or without butyrate feeding, as well as WT littermates. High working distance lens of confocal microscope was adopted to do z-stack scan of glycerol cleared whole muscles and maximal intensity projection was used to compact z-stacks into 2D images. To evaluate NMJ integrity, Alexa Fluor conjugated α-Bungarotoxin (BTX) was used to label the acetylcholine

receptors on the muscles. Neurofilament (NF) and synaptophysin (SYP) antibodies were used to label axons and axon terminals of motor neurons, respectively (**Figure 1A** and **Figure 1-figure supplement 1A**). NMJs with SYP signals present in over 60% of BTX positive area were defined as well innervated, while NMJs with SYP signals occupying less than 30% of BTX positive area were considered poorly innervated, which usually also lacked neurofilament signals in the vicinity (**Figure 1-figure supplement 1A**). The rest were considered partially innervated (**Figure 1-figure supplement 1A**). Tens to hundreds of NMJs per muscle type were measured for each mouse to calculate the ratio for the three types of NMJs (**Figure 1B** and **Figure 1-table supplement 1**). Except for EOM, EDL, soleus and diaphragm muscles from end stage G93A mice all exhibited significant decrease in the ratio of well-innervated NMJs, accompanied by dramatic increase in the ratio of poorly-innervate NMJs (**Figure 1B**). It is also worth noticing that the increase of "poorly-innervated NMJ" ratio is slightly less dramatic in diaphragm compared to the HL muscles, meanwhile the increase of "partially-innervated NMJ" ratio is the most significant in the diaphragm (**Figure 1B**), indicating the denervation process is the most severe in the HL muscles, slightly milder in the diaphragm and does not occur in the EOM. Moreover, consistent with our previous observation that NaBu treatment slows ALS progression [30], the HL and diaphragm muscles from NaBu fed mice (1 month, 2% in water) all exhibited significantly less severe denervation status (**Figure 1B**).

To confirm the image analysis results with an alternative approach, we did qRT-PCR for SCN5A, the gene encoding sodium channel Nav1.5, a marker of denervated muscles from RNAs extracted from the above types of muscles [34-36]. The results were consistent with the quantification of poorly innervated NMJ ratios **(Figure 1-figure supplement 1B** and **Figure 1-table supplement 2**). Although in this case the rescue effect of NaBu slightly missed the significance threshold for diaphragm, it is more likely just due to low sample number (it is significant when Wilcoxon ranksum test was used, but to keep the statistical method uniform across the manuscript, we only showed the t-test results).

In parallel, to quantify the abundance of SCs in the vicinity of NMJs. We did whole-mount imaging of the above types of muscles stained with SC marker Pax7, BTX, SYP and DAPI. Pax7 signals in each z-stack image were filtered using DAPI as the mask to identify nuclear $Pax7^+$ cells. Afterwards the z-stack images were compacted into 2D by maximal intensity projection (**Figure 2A**). Circles of 75 µm diameter were drawn around the NMJs and the number of nuclear $Pax7^+$ cells were counted (**Figure 2B**). Tens to hundreds of NMJs per muscle type were measured and then averaged over each mouse (**Figure 2C** and **Figure 2-table supplement 1**). Similar to the NMJ denervation status, depletion of peri-NMJ satellite cells was most significant in HL muscles from end-stage G93A mice and slightly milder in the diaphragm, while no significant depletion was observed in EOM. Intriguingly, feeding G93A mice with NaBu also improved the preservation of SCs in the HL and diaphragm muscles (**Figure 2C**).

Culturing FACS-isolated satellite cells from different muscles of wildtype and G93A mice to compare their proliferation and differentiation status

We conducted FACS based isolation of SCs from HL (combining tibialis anterior, EDL, quadriceps and gastrocnemius), diaphragm and extraocular muscles using a modified version of previously published protocol [37]. Soleus was excluded in HL muscle dissection because it has higher content of slow-twitch myofibers (40-55%), which is more similar to the diaphragm than the other four fast-twitch fiber-dominant HL muscles [38-41]. Vcam1 was used as the SC marker, while CD31 (endothelial cell marker), CD45 (hematopoietic cell marker) or Sca-1(mesenchymal stem cell marker) stained cells were discarded. Cells or debris completely unstained were also excluded. Therefore, in the FACS profile our target population ($Vcam1^+CD31^-CD45^-Sca\text{-}1^-$) was in gate P5-4 (**Figure 3A**). Single antibody staining controls were shown in **Figure 3-figure supplement 1**. We also applied methyl-green (20 µg/ml) staining [42] to evaluate the viability of cells (**Figure 3-figure supplement 2**), only about 1% of Vcam1

positive population were methyl green stained (**Figure 3-figure supplement 2D**, Events P5-2 / (P5-2 + P5-4)*100%). Thus, most cells were alive when loaded into the flow cytometer.

The SCs isolated from WT HL or diaphragm muscles exhibited relatively homogenous levels of cell surface Vcam1, making them well-separated from other cells or debris (**Figure 3A**, gate P5-4), indicating they are mostly quiescent under physiological conditions. In contrast, cell surface Vcam1 levels were more heterogeneous for SCs from G93A HL or diaphragm muscles, potentially due to constant activation and differentiation for tissue repair during disease progression (**Figure 3A**). Surprisingly, EOM SCs from both WT and G93A mice were heterogeneous in Vcam1 levels, implying these SCs can spontaneously get activated even without pathological stimulation such as denervation or muscle damage (**Figure 3A**). Additionally, statistically significant decreases of P5-4 population percentage were observed in the G93A HL and diaphragm muscle derived cells compared to WT counterparts, while no significant change was detected between G93A and WT EOM derived cells (**Figure 3B**). These results were consistent with the peri-NMJ satellite cell depletion phenotype observed in **Figure 2**.

FACS-isolated SCs were cultured in growth medium (DMEM + 20% FBS + chick embryonic extract) for 4 days and then fixed to stain for MyoD to confirm their myogenic lineage. We also looked at the ratio of actively proliferating cells (Ki67^{+}) and cells preserving nuclear Pax7. For SCs isolated from WT muscles, those derived from EOM exhibited the highest Pax/Ki67 double positive ratio. Meanwhile their Pax7/Ki67 double negative ratio was the lowest (**Figure 4A**). These observations are consistent with previous reports of superior proliferative potential of EOM SCs in culture than limb and diaphragm counterparts [24]. Interestingly, SCs derived from G93A EOM and diaphragm both exhibited high Pax7/Ki67 double positive ratio, while G93A EOM SCs had the lowest Pax7/Ki67 double negative ratio (**Figure 4A**). The higher Pax7/Ki67 double positive ratio and lower Pax7/Ki67 double negative ratio of cultured G93A diaphragm SCs compared to WT counterparts may reflect a counteracting mechanism against SC depletion during ALS progression (**Figure 4-figure supplement 1A**), yet this does not seem to be supported by RNA-Seq and qRT-PCR results described later.

Next, we examined the status of myotube formation, stemness preservation and cell proliferation of cultured SCs under differentiation conditions. After the 4-day culture in growth medium, we switched to low serum medium (DMEM + 2% HS) and culture for 2 more days. The cells were fixed and stained for sarcomere myosin heavy chain (MHC), Pax7 and Ki67. EOM SCs exhibited the highest Pax7/Ki67 double positive ratio compared to their HL and diaphragm counterparts in either the WT or the G93A group (**Figure 4B**), demonstrating a superior capability to preserve renewability and stemness in a differentiation-preferrable environment. In contrast, the fusion indices, which calculate the ratio of nucleus within the MHC positive myotubes, were the lowest for EOM SCs (**Figure 4B**). This does not necessarily mean the EOM SCs have deficiencies in differentiation after they are committed, but more likely a reflection of their superior preservation of actively proliferating population [43]. In support of this view, previous TA engraftment experiments showed that more myofibers were generated by EOM SCs than their limb counterparts [24].

Butyrate induced EOM-like changes in the homeostasis of FACS-isolated SCs under differentiation conditions

Since NaBu feeding ameliorated SC depletion in end stage G93A mice, we wonder if NaBu treatment of cultured SCs could directly impact their homeostasis. To assess the optimal concentration of NaBu to administer, we cultured G93A HL SCs with 0 mM, 0.1 mM, 0.5 mM, 1 mM, 2.5 mM and 5 mM of NaBu in growth medium for 1 day. RNAs were collected for qRT-PCR to evaluate the short-term impact of NaBu on cell growth. Interestingly, the relative quantities of both HMGA2 and CCND1 transcripts (proliferation markers) take on a concave-down shape along the dose series which peaked

at 0.5 mM concentration. In contrast, the relative quantities of proliferation inhibitor P21 form a concave-up curve that bottomed at 0.5 mM (**Figure 5A**). As to the timing and duration of NaBu treatment, previous studies with C2C12 cells suggested transient exposure (1 day) in growth medium before the induction of differentiation would enhance the differentiation process, while the addition of NaBu to the differentiation medium has the opposite effect [28]. Thus, we adopted two treatment plans for G93A diaphragm and HL SCs: one with 0.5 mM NaBu applied in the growth medium for 1 day before switching to normal differentiation medium (Day 4 of culture). The other with 0.5 mM NaBu continuously applied for 3 days from the day before switching to differentiation medium (Day 4 to Day 6 of culture). We observed a treatment duration-dependent increase in the preservation of $Pax7^+$ cells, as well as a treatment duration-dependent decrease of fusion indices. The 3-day NaBu treatment plan increased both the Pax7/Ki67 double positive ratio and the $Pax7^+/Ki67^-$ ratio in cultured G93A HL and diaphragm SCs, while the 1-day NaBu treatment plan did not significantly improve the Pax7/Ki67 double positive ratio of G93A HL SCs in culture. For the 3-day NaBu treatment plan, aside from the drop of fusion indices, we also observed notable decrease of MHC levels in myotubes, indicating long-term exposure to NaBu did inhibit the differentiation process (**Figure 5B**).

Comparing transcriptome profiles of SCs from different origins cultured in growth and differentiation medium with or without butyrate

To identify the potential transcriptomic features linked with the superior renewability and stemness preservation nature of EOM SCs, we extracted RNAs from HL, diaphragm and EOM SCs under the following two culture conditions:1. In growth medium for 4 days (with suffix “G”); 2. In growth medium for 4 days and then in differentiation medium for 2 days (with suffix “D”). After quality checking, the RNAs were send for bulk RNA-Seq. We also did RNA-Seq for G93A HL and diaphragm SCs experienced 3-day NaBu treatment (with suffix “NaBu3”) or 1-day NaBu treatment. Because there were too few differentially expressed genes between the samples with 1-day NaBu treatment and non-treated controls, we excluded these samples from the analysis described below, but the original BAM files are available in the GEO database for readers of interest.

Several key discoveries were made when we checked the similarities between the gross transcriptomic profiles of our RNA-Seq samples using unsupervised approaches such as PCA analysis and hierarchical clustering (**Figure 6A**): 1. EOM SCs cultured in differentiation medium were more similar to HL and diaphragm SCs in growth medium than their counterparts in differentiation medium. This is consistent with the immunostaining results showing superior capability of EOM SCs to preserve renewability and stemness in differentiation medium. 2. The 3-day NaBu treatment shifted the transcriptomic profile of G93A HL and diaphragm SCs closer to those SCs cultured in growth medium, confirming the stemness preservation and differentiation inhibition effect of NaBu. 3. For SCs derived from end stage G93A mice and WT controls cultured under the same conditions, as long as they were of the same muscle origin, their transcriptomic profiles were relatively similar. Thus, the SC behavior and abundance changes in vivo are more likely a response to ALS pathogenesis.

To better understand the RNA-Seq data in the perspective of SC homeostasis [43], we compiled our lists of quiescence signature genes, activation signature genes and differentiation signature genes, respectively. For quiescence signature genes, a list of 507 genes highly upregulated (over 5-fold) in quiescent SCs compared to activated SCs have been generated previously by Fukada et al [44], we adopted this list (except two of them: one with Genbank ID AA266723, which we cannot find corresponding gene ID; the other one with Genbank ID BB471309, which belongs to the gene *Cbfa2t3* already in their list) and 18 genes denoted in other papers, including *Notch1*, *Notch2*, *Hes1*, *Hey1*, *Rbpj*, *Dtx4*, *Jag1*, *Sox8*, *Sdc3*, *Itga7*, *Itgb1*, *Met*, *Vcam1*, *Ncam1*, *Cdh2*, *Cdh15*, *Cxcr4*, *Cav1* [43,45-48]. For the activation and differentiation signature genes, our RNA-Seq data showed that SCs cultured in

growth medium and differentiation medium had distinct gene expression profile (**Figure 6-figure supplement 1A**). We generated the activation signature gene list from those expressed significantly higher in SCs isolated from every type of muscle (both from WT and G93A mice) in growth medium ($|\log2FC| \geqslant 0.4$ and FDR $\leqslant 0.001$, 1187 genes in total). Accordingly, the differentiation signature genes are those expressed significantly higher in SCs cultured in differentiation medium (1349 genes in total). To verify that our signature gene lists recapture the SC properties at activation and differentiation state reported in previous studies, we did functional annotation analysis (KEGG pathway, Gene ontology_biological process, Gene ontology_cellular component). The top functional annotations enriched in our activation signature genes are related to cell cycle and DNA replication, while the top functional annotations for our differentiation signature genes are associated with muscle contraction, muscle-specific subcellular structures and metabolic changes (**Figure 6-figure supplement 1B**). Through screening for members of these three categories in a differentially expressed gene (DEG) list between two samples and examining their expression change direction and fold, we would be able to tell the homeostasis preferences of these two samples.

To explore whether the homeostasis preferences of EOM SCs are different from SCs derived from other muscles, we looked for DEGs shared-in-common between the following four comparing groups: WT EOM SC-vs-WT diaphragm SC; WT EOM SC-vs-WT HL SC; G93A EOM SC-vs-G93A diaphragm SC; G93A EOM SC-vs-G93A HL SC (**Figure 6B**, left two panels). Within 1119 shared DEGs identified in SCs cultured in growth medium, slightly more activation signature genes and quiescence signature genes were expressed higher in EOM SCs compared to diaphragm and HL derived counterparts. Meanwhile more differentiation signature genes were expressed lower in EOM SCs (**Figure 6C**, leftmost panel). These trends became much more prominent in the 3318 shared DEGs identified in SCs cultured in differentiation medium, implying EOM SCs in differentiation medium are notably superior at preserving renewability and stemness in a differentiation-favoring environment than their diaphragm and HL counterparts (**Figure 6C**, middle panel). Consistently, subgroups of quiescence signature genes belonging to commonly used stem cell markers (*Pax7, Cd34, Cxcr4, Vcam1, Sdc3, Sdc4, Cdh15, Met, Cav1*), Notch signaling pathway (*Notch1, Notch2, Notch3, Jag1, Heyl, Dtx4, Msc*) and pluripotency signaling pathway (*Klf4, Igf1, Bmp2, Bmp4, Fzd4, Fgfr4, Pik3r1, Lifr*) were all expressed higher in EOM SCs in differentiation medium than diaphragm and HL SCs (**Figure 6C**, middle panel and **Figure 6-table supplement 1**). In contrast, no Notch signaling component was expressed universally higher in EOM SCs than their diaphragm and HL counterparts cultured in growth medium (**Figure 6-table supplement 2**).

In parallel, we examined the homeostasis preferences of diaphragm and HL SCs with or without the 3-day NaBu treatment (**Figure 6B**, rightmost panel). There were 3018 DEGs shared between the following two comparing groups: G93A diaphragm SC_D_NaBu3-vs-G93A diaphragm SC_D and G93A HL SC_D_NaBu3-vs-G93A HL SC_D. Similar to the trends observed in EOM SCs in differentiation medium, the majority of activation and quiescence signature genes found in these DEGs were upregulated in the NaBu treated group, while the opposite was true for the differentiation signature genes (**Figure 6C**, rightmost panel). The elevated quiescence signature genes of the NaBu treated group include commonly used stem cell markers (*Pax7, Cd34, Vcam1, Sdc4, Cdh2, Met, Cav1, Itga7*), Notch signaling pathway members (*Notch3*, *Rbpj*) and pluripotency signaling pathway components (*Fzd4*, *Bmp4*). Yet other three pluripotency related genes (*Klf4*, *Wnt4* and *Bmp2*) were found downregulated (**Figure 6-table supplement 3**).

Aside from analyzing the homeostasis status, we also aim to do functional annotation analysis of genes expressed higher in EOM SCs than counterparts from other muscles. To compile this gene list, we first identified the 621 genes expressed higher in EOM SCs than diaphragm and HL counterparts cultured in growth medium from the 1119 DEGs highlighted in the leftmost panel of **Figure 6B**. Next,

we pulled out 2424 genes expressed higher in EOM SCs than diaphragm and HL counterparts cultured in differentiation medium from the 3318 DEGs shown in the middle panel of **Figure 6B**. These two lists have 478 genes shared-in-common. Very interestingly, many of these genes are related to axon guidance, cell migration and neuron projection (**Figure 7A**, **Figure 7A-figure supplement 1**, **Figure 7-table supplement 1 and 2**). More intriguingly, when we conducted functional annotation analysis for the 3018 genes altered by the 3-day NaBu treatment (**Figure 6B**, rightmost panel), we also spotted axon guidance, cell migration and neuron projection on the top of the annotation lists (**Figure 7B** and **Figure7-table supplement 3**). The chemokine *Cxcl12* shows up in all three lists and is known to be produced by perisynaptic Schwann cells after acute motor axon terminal degeneration to promote directional axonal extension and NMJ regeneration [49]. Thus, enhanced attraction of motor neuron axons by peri-NMJ SCs might be a mechanism shared-in-common between the superior NMJ integrity of EOMs in end stage G93A mice and NaBu mediated amelioration of denervation.

To confirm the results of homeostasis status and functional annotation analyses above, we selected one representative gene from each of the following categories: activation signature gene (*Hmga2*), differentiation signature gene (*Actn3*), quiescence signature gene (*Notch3*) and axon guidance gene (*Cxcl12*) for qRT-PCR. For each muscle type and culture condition, we collected samples from 3-6 rounds of sorting (sorted cells were split into 3 replicates, **Figure 7C-E** and **Figure 7-table supplement 3-5**). We observed significantly higher expression of *Hmga2* in EOM SCs compared to diaphragm and HL counterparts cultured in either growth or differentiation medium (**Figure 7C**, leftmost panel), confirming the superior renewability of EOM SCs. The 3-day NaBu treatment of diaphragm and HL SCs derived from G93A mice also upregulated *Hmga2* (**Figure 7D**, leftmost panel). The differentiation marker *Actn3* was expressed lower in EOM SCs than diaphragm SCs cultured in either growth or differentiation medium, but not necessarily lower than HL counterparts (**Figure 7C**, 2nd panel from the left). Meanwhile NaBu treatment significantly decreased *Actn3* expression (**Figure 7D**, 2nd panel from the left). This observation partially supports the interpretation made earlier in describing the immunostaining results of cultured SCs: 3-day NaBu treatment does inhibit differentiation (weaker MHC levels in myotubes) but EOM SCs do not necessarily have deficient differentiation when they are committed (MHC levels in myotubes comparable to those of other muscle origins). The lower expression of differentiation markers in EOM SCs is indirectly caused by the high proportion of actively proliferating cells. Consistent with the RNA-Seq data, the quiescence marker *Notch3* was expressed significantly higher in EOM SCs than diaphragm and HL counterparts cultured in differentiation medium but not in growth medium (**Figure 7C**, 2nd panel from the right). Meanwhile NaBu treatment also elevated *Notch3* expression (**Figure 7D**, 2nd panel from the right), confirming its stemness preservation effect. Last but not the least, the axon guidance molecule *Cxcl12* was expressed significantly higher in EOM SCs than their diaphragm and HL counterparts cultured in both growth and differentiation medium (**Figure 7C**, rightmost panel). NaBu treatment elevated *Cxcl12* expression as well (**Figure 7D**, rightmost panel), confirming enhanced axon attraction as a common feature shared by EOM SCs and NaBu treatment.

AAV mediated overexpression of *Cxcl12* promotes motor neuron axon extension and partially mimic the multi-innervation property of EOM SC derived myotubes

Since recombinant *Cxcl12* protein was known to promote axon extension previously [49], we moved forward to test whether overexpressing *Cxcl12* in myotubes through adeno-associated virus (AAV) transduction could achieve the same effect using compartmentalized microfluidic chamber (XonaChip, with 450 μm microgroove barrier between two compartments). This assesses the possibility of developing muscle-derived *Cxcl12* as a gene therapy tool against denervation. Because AAV vectors, even the most muscle-tropic serotypes like AAV6, AAV8 and AAV9, do not transduce satellite cells efficiently [50,51], we seeded satellite cells first into one compartment of XonaChip and induce them to differentiate for two days before conducting AAV transduction. Four types of AAV-transduced myotubes

were used for the coculture assays: 1. WT HL SC-derived myotubes transduced with AAV-CMV-eGFP; 2. G93A HL SC-derived myotubes transduced with AAV-CMV-eGFP; 3. G93A HL SC-derived myotubes transduced with AAV-CMV-Cxcl12-IRES-eGFP; 4. G93A EOM SC-derived myotubes transduced with AAV-CMV-eGFP. One day after the AAV transduction, rat spinal motor neurons (RSMNs) were seeded into the other compartment of the chamber and the culture medium was switched to Neurobasal Plus Medium (NBPM) (**Figure 8A**). The coculture system was maintained for 9 more days with medium change every 2 days. Immunostaining confirmed increased presence of Cxcl12 protein in myotubes transduced with AAV8-CMV-Cxcl12-IRES-eGFP but not those transduced with AAV8-CMV-eGFP (**Figure 8-figure supplement 1**). It is worth noticing that the Cxcl12 protein detected by immunostaining were mostly enriched in perinuclear region, likely inside lysosomes due to autophagy activated by AAV-mediated over-abundant production [52], while secreted or cytosolic Cxcl12 protein were harder to detect. Additionally, the cells we can acquire in each sort is relatively limited. That is why we used more sensitive assays like qRT-PCR rather than immunostaining or Western blot for validating *Cxcl12* expression earlier in this manuscript.

When we measured the lengths of the longest RSMN neurites (presumably axons) crossing the 450 μm microgrooves, we noticed that G93A HL SC derived myotubes were slightly repulsive to axon extension compared to their WT counterparts (both myotubes overexpress GFP). In many cases, the axons stayed close to the edges of the microgrooves and even grew backward towards the neuronal compartment, which we nick-named “edge effect” (**Figure 8B** and **Figure 8-figure supplement 2A**, arrows). In sharp contrast, RSMN axon extension was dramatically enhanced in cocultures either with G93A HL SC-derived myotubes overexpressing *Cxcl12* or G93A EOM SC-derived myotubes overexpressing GFP (**Figure 8B, D**). Those myotubes located close to the microgrooves constantly got entangled by neurites (**Figure 8-figure supplement 2B**). Intriguingly, G93A HL SC-derived myotubes overexpressing *Cxcl12* were even seen to overcome the “edge effect” and redirect the axons towards their proximities (**Figure 8-figure supplement 2B**, arrow), which is a persuasive indicator of chemoattraction. Meanwhile, RSMN innervation of AChR clusters (BTX positive patches) were not seen in cocultures with G93A HL SC-derived myotubes overexpressing GFP, but observed in the rest three types of AAV-transduced myotubes (**Figure 8C**). Yet the overall innervation incidence was too low for statistical analysis, at least partially due to the sparsity of axons in the myotube compartment. To solve this issue, we cocultured mouse myotubes with rat spinal motor neurons within the same compartment in the following assays, with the same timeline of procedures.

Under the uni-compartmental coculture setting, the innervation ratios of AChR clusters in HL SC-derived myotubes (overexpressing GFP) having contacts with RSMN neurites were not significantly different between WT and G93A mice. In contrast, *Cxcl12* overexpressing G93A HL myotubes indeed exhibited higher innervation ratio than GFP overexpressing counterparts (**Figure 9A-C** and **Figure 9-figure supplement 1A-C**). Shockingly, this improvement was dwarfed by what occurred in RSMNs cocultured with G93A EOM SC-derived myotubes, in which individual myotubes were frequently observed to be innervated 3 or more times (**Figure 9A-C** and **Figure 9-figure supplement 1D**), potentially due to the preservation of the “multi-innervation” property of EOM reported in vivo [3]. These extra “anchor points” seem to enhance the tethering of RSMN axons to myotubes, aligning the axon network to the spatial configuration of myotubes on a global scale. On the contrary, the axon network of RSMNs cocultured with HL SC-derived myotubes did not appear to be spatially correlated with myotube patterns (**Figure 9A-C** and **Figure 9-figure supplement 1A-C**). Furthermore, in zoom-in views we constantly observed axons ramify to send projections to adjacent BTX positive patches on EOM SC-derived myotubes (**Figure 9B**, arrows), which implicated axon branching during innervation. More than a coincidence, several Netrin and Semaphorin family members reported to promote axon-branching were spotted in the signature gene lists of differentiated EOM SCs (**Figure 7-table supplement 2**) [53-58]. They may help explain the notably high innervation ratio of EOM SC-derived

myotubes. Thus, the production of a cocktail of axon guidance molecules, in combination with the robust self-renewability of satellite cells, may contribute to the ALS resistant nature of EOM.

Discussion

In this study we first detected an association between the degeneration of NMJs in HL and diaphragm muscles in end-stage G93A mice and depletion of peri-NMJ SCs. In contrast, NMJs in EOM exhibit no signs of denervation or SC depletion. The FACS profile of SCs isolated from EOM cues for occurrence of spontaneous activation even without pathological stimulation, which is supported by previous in vivo BrdU labeling and staining results [59]. Meanwhile immunostaining, qRT-PCR and RNA-Seq analysis all imply that EOM SCs in culture possess superior renewability and preserve stemness better under the pressure of differentiation than HL and diaphragm counterparts. Furthermore, comparative functional annotation analysis highlights more abundant presence of axon guidance molecules in the transcriptome of EOM SCs. Neuromuscular co-culture experiments demonstrate that EOM SC-derived myotubes are more attractive to potential axons derived from rat spinal motor neurons than their HL counterparts. Thus, the unique homeostasis regulation and axon attraction properties of EOM SCs may contribute to the resistance to denervation and SC depletion in EOM under ALS (**Figure 9D**).

The abundance and proliferation/differentiation abilities of SCs derived from ALS donors and mice models have been assessed in multiple studies previously [60-65]. For human studies, the earliest report of SC quantity from muscle biopsy samples using electron microscopy detected no significant difference between ALS patients and controls without neuromuscular disorder [60]. Two other studies using primary cultured SCs from muscle biopsy samples implied compromised differentiation program in ALS SCs compared to controls [61,62]. As to proliferation, one study reported enhanced proliferation in ALS SCs [61], while the other cued for deficits in proliferation in ALS SCs due to the upregulation of P16 (a negative regulator of proliferation) [62]. The conflicts in these results may result from the lack of FACS isolation based on SC specific markers and hence the extent of contamination by other cell types may vary. Additionally, variations in the disease stage of patients cannot be controlled during sampling. For animal studies, Manzano et al measured the amount of Pax^{7+} SCs in dissociated EDL and soleus myofibers from $SOD1^{G93A}$ mice and WT controls. However, no uniform trend of increase or decrease could be identified. Rather, the abundance of SC seems to vary drastically across muscle-type and disease stage [65]. In another study carried out by the same group, primarily cultured EDL and soleus SCs from $SOD1^{G93A}$ mice generally showed lower proliferation potential than the WT counterparts. In our whole-mount muscle imaging data and FACS profile of isolated SCs, SC depletion is evident in HL and diaphragm muscles from end-stage G93A mice and the severity is higher in HL muscles than diaphragm. This could either be due to the distal-to-proximal progression order of the disease or relatively higher renewability of diaphragm SCs than HL counterparts. Additionally, the FACS profiles of HL and diaphragm SCs derived from WT mice show relatively homogenous levels of Vcam1, implying most cells are quiescent. In contrast, the Vcam1 levels of HL and diaphragm SCs derived from end stage G93A mice are heterogenous, indicating they are at least partially activated, likely due to the pathological stimulations under ALS. Although this activation may transiently elevate the number of SCs, overtime they will differentiate into myotubes. Taking naturally occurring cell death into consideration, the quiescent stem cell pool will gradually get exhausted due to the dominance of asymmetric over symmetric cell division, leading to the depletion phenotype seen in end stage G93A mice. In contrast, the superior preservation of renewability and stemness of EOM SCs under differentiation pressure is an effective preventive measure against this catastrophe. When FACS-isolated SCs derived from WT or G93A mice were treated under the same culture condition, those derived from the same muscle type

generally have similar gene expression profile and proliferation/differentiation behavior. The G93A diaphragm SCs cultured in growth medium may seem more proliferative than the WT counterparts in immunostaining. But we do not see consistently higher expression of proliferation markers in RNA-Seq or qRT-PCR data. Thus, we do not consider it conclusive that G93A diaphragm SCs have higher renewability than WT counterparts.

Cxcl12 has been known as a critical axon guidance cue for motor neurons during development [66,67]. Axons of ventral motor neurons exiting the neural tube transiently express high levels of Cxcr4, which respond to the *Cxcl12* produced from the surrounding mesenchymal cells. In mouse embryos with mutant *Cxcr4* or *Cxcl12*, many axons of ventral motor neurons take abnormal trajectories towards the dorsal side [66]. *Cxcr4/Cxcl12* signaling has also been reported to mediate the initial pathfinding of oculomotor axons and direct their proper innervation of the extraocular muscles. In adult animals, peri-synaptic Schwann cells have recently been reported to transiently produce *Cxcl12* after acute motor axon terminal degeneration. Intraperitoneal injection of antibodies neutralizing secreted Cxcl12 protein slows down the regeneration process. In contrast, the exposure of primary motor neurons to recombinant Cxcl12 protein stimulates neurite outgrowth and directional axonal extension in compartmentalized culture setup, which could be reversed by the treatment of the Cxcr4 specific inhibitor AMD3100 [49]. Since myoblasts also express *Cxcr4* and will migrate along the Cxcl12 protein gradient during muscle regeneration [68,69], the abundant peri-NMJ SCs in EOM expressing *Cxcl12* may achieve synergistic effect with peri-synaptic Schwann cells, improving the long-term integrity of NMJs.

NaBu is a gut-bacteria fermentation product that can inhibit histone deacetylase (HDAC) activities and act as an energy source to improve mitochondrial respiration [25,70]. Our previous study showed NaBu feeding significantly prolonged the life span of G93A mice and reversed CypD-related mitoflash phenotypes in flexor digitorum brevis myofibers derived from G93A mice, which implies a potential decrease of oxidative stress. Additionally, NaBu treatment also improved mitochondrial respiratory function of NSC34 motor neuron cell line overexpressing hSOD1G93A [30,32,33]. The study here revealed its beneficiary effect on the preservation of NMJ integrity and peri-NMJ SCs during ALS progression. NaBu treatment of G93A HL and diaphragm SCs in culture induced transcriptomic changes mimicking some features seen in EOM SCs, including the upregulation of activation and quiescence signature genes and the downregulation of differentiation signature genes. Some axon guidance molecules, like *Cxcl12*, were also induced by NaBu (**Figure 9D**). It is worth clarifying that we did not include NaBu treatment in the neuromuscular coculture experiments because NaBu has been reported to affect axonal transport by inhibiting HDAC6 [25,71]. These effects will interfere with our aim to specifically evaluate how myotube-derived factors affect axon length and innervation ratios.

It is also worth mentioning that a cocktail of sodium phenylbutyrate (a derivative of NaBu) and Taurursodiol (an antioxidant) has been approved by US and Canada for the treatment of ALS last year under the Commercial name Relyvrio [72]. We believe there are timely needs for mechanistic studies of butyrate derivatives, which could help scientists and public audience gain more insights into the biological impacts of this type of treatment.

Materials and methods

Animals

All animal experiments were carried out in strict accordance with the recommendations in the *Guide for the Care and Use of Laboratory Animals* of the National Institutes of Health. The protocol on the usage of mice was approved by the Institutional Animal Care and Use Committee of the University of Texas

at Arlington (A19.001, approval date: 09/20/2018). Wild-type mice used in this study were of B6SJL background. The ALS transgenic mouse model (hSOD1G93A) with genetic background of B6SJL was originally generated by Drs. Deng and Siddique's group at Northwestern University and deposited to the Jackson Lab as B6SJL-Tg (SOD1*G93A). For the butyrate feeding experiment, the animals were fed with 2% NaBu from the age of 3 months (at the ALS disease onset) [31,73,74] and lasting for 4 weeks.

Primary culture of satellite cells isolated by fluorescence-activated cell sorting

For hindlimb muscles, tibialis anterior (TA), extensor digitorum longus (EDL), gastrocnemius, and quadriceps were dissected from 1-2 mice. For diaphragm, both the crural and costal domains were dissected from 1-2 mice. For EOM, the four rectus muscles in the eye sockets were dissected from 5-6 mice. The collected muscles were placed in 0 mM Ca^{2+} Ringer's solution. Excessive connective tissue, tendons, fat, blood clots, vessels and hairs were removed as much as possible. After cleanup, the muscles were transferred into the digestion media (DMEM containing 5% FBS, 1% Pen/Strep and 10 mM HEPES) and minced into small blocks using scissors. Collagenase II (Worthington LS004176), dispase II (Sigma D46931G), hyaluronidase (Worthington LS002592) and Dnase I (Worthington LS002139) were added at the final concentration of 0.26%, 0.24%, 0.16% and 0.04%, respectively. The digestion system was placed in an orbital shaker running at 70 rpm at 37 °C for 45 min. The digested muscles were triturated 10 times with a 20-gauge needle attached to a 5 ml syringe. Afterwards the triturated mixture was pipetted onto a pre-wetted 100 µm strainer and centrifuge at 100 g for 2.5 min to precipitate the bulky myofiber debris. The supernatant was transferred onto a pre-wetted 40 um strainer and cells were collected by centrifuged at 1200 g for 6.5 min. The cells were resuspended in sorting media (PBS containing 0.3% BSA, 10 mM HEPES and 1 mM EGTA) and stained with antibodies or dyes at 4 °C for 45 min with shaking. The antibodies used include: PE anti-mVcam1 (Biolegend 50604858, 600 ng/10^6 cells), APC anti-mCD31 (Biolegend 50162682, 400 ng/10^6 cells), APC anti-mCD45 (Biolegend 50162782, 400 ng/10^6 cells) APC anti-mSca-1 (Biolegend 50163216, 200 ng/10^6 cells). This antibody combination followed a previous published protocol [37]. Vcam1 is a SC marker, CD31 is a endothelial cell marker, CD45 is a hematopoietic cell marker and Sca-1 is a mesenchymal stem cell marker [37]. For sorting, our target population is $VCAM^+CD31^-CD45^-Sca\text{-}1^-$. When needed, the cells were stained with methyl green (2 µg/ml) to check mortality rate. As a positive control, half of the cells were transferred to a new Eppendorf tube and methanol (precooled at -20°C) was added dropwise with gentle mixing and left on ice for 5 min, the dead cells were wash twice before being mixed with the rest half of cells for methyl green staining. The sorting process was conducted using BD FACS Melody Cell Sorter using a 100 µm nozzle. The excitation laser and emission filter setup for methyl green is the same as APC. The flow rate was tuned between 1-7 to adjust the event rate to 2000-4000/sec. Gating conditions of FSC-A/SSC-A, SSC-H/SSC-W, FSC-H/FSC-W, Vcam1/CD31_CD45_Sca-1 and Vcam1/Methyl green plots were shown in Figure 3-figure supplement 1 and Figure 3-figure supplement 2. The sorted cells were collected in growth media (DMEM containing 20%FBS, 1% Pen/Strep, 1% chick embryonic extract and 10 mM HEPES). Afterwards the cells were seeded into laminin (Corning 354232) -coated plates or glass-bottom dishes containing growth media (without HEPES). Culture media was changed on the third day and the fourth day. To induce differentiation, cells were washed three times with PBS and cultured in differentiation media (DMEM containing 2% horse serum) for 2 more days.

Neuro-muscular co-culture assay

For neuromuscular co-culture in compartmentalized chambers (XonaCHIPS XC450), XoanCHIPS were coated with poly-L-ornithine (0.5 mg/ml) for 1 hr at 37 °C followed by laminin (0.1 mg/ml) for 1 hr at 37 °C. Primarily cultured satellite cells were seeded at 1x10^5 into the myotube compartment in growth medium for attachment overnight and then switched to differentiation medium and cultured for

2 more days. Afterwards AAV8-CMV-eGFP (Vector Biolabs, 1x10^11 GC/ml) or AAV8-CMV-Cxcl12-IRES-eGFP (Vector Biolabs, 1.5x10^11 GC/ml, the *Cxcl12* gene is of mouse origin) transduction was conducted for one day. The usage of higher titer for the second virus is for matching GFP signal intensity, as IRES-dependent expression is significantly lower than those directly driven by CMV [75]. The chambers were washed with Neurobasal Plus Medium twice before seeding rat spinal motor neurons into the neuronal compartment (1x10^5). The co-culture was kept in Neurobasal Plus Medium for 9 more days and half medium change was conducted every 2 days.

For neuromuscular co-culture in the same glass-bottom chamber, 8-well chambered cover glasses (Cellvis C8-1.5H-N) were coated with poly-L-ornithine and laminin as described above. Primarily cultured satellite cells were seeded at 1x10^5/chamber in growth medium for attachment overnight and then switched to differentiation medium and cultured for 2 more days. AAV transduction was conducted for one day as described above. The infected myotubes were washed with Neurobasal Plus Medium (Thermo Fisher A3582901, with B-27 and GlutaMax supplement) before the addition of rat spinal motor neurons (4x10^3/chamber, iXCells 10RA-033) to the same chamber. The co-culture was kept in Neurobasal Plus Medium for 9 more days and half medium change was conducted every 2 days.

Immunofluorescence (IF) and imaging of whole mount muscle samples

EDL, soleus and EOM (the four rectus muscles) were dissected out and fixed in 4% paraformaldehyde (PFA) for 1 hr. Afterwards the samples were washed with PBS containing 1% glycine once and two more times with PBS. Further fixation and permeabilization was done with methanol at -20°C for 10 min. For diaphragm, the costal muscles and their surrounding rib cages were dissected and immersed in methanol directly for fixation (PFA fixation was skipped because it made the diaphragm harder to flatten and introduced more non-specific noises in staining). The samples were rehydrated and washed with PBS. The epimysium and tendons were removed as much as possible. EDL and soleus were further split into smaller bundles along the longitudinal axis. Then the samples were immersed in blocking buffer (PBS containing 2% BSA, 2% horse serum, 0.1% Tween-20, 0.1% Triton X-100 and 0.05% sodium azide) overnight at 4 °C. Next day the samples were incubated with primary antibodies for 1-2 days. After washing with PBS for three times, the samples were incubated with Alexa Fluor labelled secondary antibodies (Thermo Fisher 1:1000) and Alexa Fluor 488 conjugated α-Bungarotoxin (Thermo Fisher B13422, 1:1000) for 1-2 days. The samples were then washed with PBS, counterstained with DAPI and mounted in antifade mounting media (20 mM Tris, 0.5% N-propyl gallate, 80% glycerol) for imaging. Primary antibodies used: neurofilament (DSHB 2H3 concentrate, 1:250), synaptophysin (Fisher PA11043, 1:400), Pax7 (SCBT sc-81648, 1:100), Pax7 (Thermo Fisher PA1-117, 1:200), CXCL12 (R&D MAB350, 1:200).

To quantify SC number surrounding NMJs, z-stack images were compacted using maximum projection and circles (75 µm in diameter) were drawn around each NMJ in Image J. The DAPI channel was used as a mask to filter out nonspecific staining of Pax7 in the extracellular matrix.

IF and Imaging of cultured myoblasts/myotubes and motor neurons

The cells were fixed in 4% PFA for 10 min and then washed with 1% glycine and PBS. Further fixation and permeabilization was done either with methanol at -20°C for 10 min or 0.25% TritonX-100 for 15 min. The samples were then washed with PBS and immersed in blocking buffer for 40 min. Primary antibody incubation was done at 4 °C overnight. Next day the cells were washed with PBS and incubated with Alexa Fluor labelled secondary antibodies (1:1000) for 2 hours at room temperature, counterstained with DAPI and mounted in antifade mounting media for imaging. Primary antibodies used: Alexa Fluor647 conjugated α-Bungarotoxin (Thermo Fisher B13422, 1:1000), Pax7 (SCBT sc-81648, 1:100), MyoD (SCBT sc-377460, 1:100), Ki-67 (CST 12202S, 1:300), MYH (DSHB MF20

concentrate, 1: 200), neurofilament (DSHB 2H3 concentrate, 1:250), eGFP (Novus NBP-22111AF488, 1:250).

For quantifying innervation ratio, AChR clusters (BTX patches) larger than 10 μm^2 were counted on myotubes that have contact with RSMN neurites. Those myotubes having 0 pixel overlap with RSMN neurites were not included in measurement. The ratio of AChR clusters having overlaps with the RSMN neurites after visual inspection of the whole z-stacks of each view were calculated. The innervation ratio of each view is one dot in the box-and-dot plot in Figure 9C. The measurements were done for 3 rounds of coculture assays.

RNA extraction and qRT-PCR

For cultured SCs, cell culture medium was removed before RNA extraction and Trizol reagent was added to the well before scratching cells off using pipette tips. The homogenate was transferred into tubes containing 5 PRIME Phase Lock Gel (Quantabio 2302830), and 1/10 volume of 1-bromo-3-chloroporpane (Alfa Aesar A11395) was added. The samples were shaken vigorously for 12 s and centrifuged for 15 min at 16,000× *g*. Afterwards, the upper phase was transferred to another Eppendorf tube and isopropanol (1/2 volume of the initial homogenate) was added for precipitation overnight at −20 °C. Next day, after 15 min centrifugation at 16000 *g* the precipitate was washed briefly with 75% ethanol. After another 5 min centrifugation, the ethanol was removed. The precipitate was briefly dried and resuspended in RNase free water. For whole muscle samples, the freshly dissected muscles were snap-frozen in liquid nitrogen, kept at -80 °C freezer overnight and then soaked in RNALater ICE (Thermo Fisher AM7030) for 2-3 days at -20 °C. Before RNA extraction, leftover tendons and axons were removed and muscles were transferred to 1 ml Trizol. Homogenization was conducted in FastPrep-24 Classic bead beating grinder (MP Biomedicals 116004500). The tissue homogenate was transfer to centrifuge tubes containing phase lock gel (QuantaBio 2302830) and 1/10 volume of 1-bromo-3-chloropropane was added. The tubes were hand shaken for 12 seconds, left at bench top for 2 minutes and then centrifuged at 16000 g at 4 °C for 15 minutes. The upper phase was transferred to a new centrifuge tube and mixed with equal volume of ethanol. The following steps of RNA purification was conducted with Direct-zol RNA Miniprep Plus kit (Zymo Research R2070). RNA concentration was measured with Quantus Fluorometer (Promega E6150). RNA quality was assessed by RNA ScreenTape analysis at Genomics Core Facility at the University of North Texas Health Science Center. Only RNAs with RIN ≥ 9 and 28s/18s ≥ 1 were used for qRT-PCR or RNA-Seq. Reverse transcription was done using Promega GoScript Reverse Transcription system. The qPCR reactions used Maxima SYBR Green/ROX qPCR Master Mix (Thermo Fisher) and were carried out by the StepOnePlus Real-Time PCR system (Thermo Fisher). Relative quantification (RQ) of gene expression was generated by ΔΔCt method. The sequences of primers used for qPCR were listed in Table 1.

Table 1. qPCR primer sequences.

Target gene	Forward primer	Reverse primer
Actn3	AACAGCAGCGGAAAACCTTCA	GGCTTTATTGACATTGGCGATTT
Cxcl12	TGCATCAGTGACGGTAAACCA	TTCTTCAGCCGTGCAACAATC
Gapdh	AGGTCGGTGTGAACGGATTTG	TGTAGACCATGTAGTTGAGGTCA
Hmga2	GAGCCCTCTCCTAAGAGACCC	TTGGCCGTTTTTCTCCAATGG
Notch3	GGTAGTCACTGTGAACACGAGG	CAACTGTCACCAGCATAGCCAG
Scn5a	ATGGCAAACTTCCTGTTACCTC	CCACGGGCTTGTTTTTCAGC

Bulk RNA-Seq and analysis

Non-stranded mRNA sequencing was carried out by BGI Americas Corporation. The average number of clean reads per sample was 45.16 million (ranging from 44.11 to 48.51 million). The average percentage of clean reads was 93.32% (ranging from 92.42% to 93.97%). The average percentage of aligned reads (to Genome Reference Consortium Mouse Build 38 patch release 6) was 96.01% (ranging from 95.40% to 96.67%) and the average percentage of uniquely aligned reads was 86.46% (ranging from 85.12% to 87.63%). To identify differentially expressed genes (DEGs) between different samples (using Poisson distribution method to compare uniquely mapped reads of the gene), only genes with $|\log2FC| \geq 0.4$ and FDR ≤ 0.001 were considered. To identify DEGs between different groups (containing more than one sample, using DESeq2 method), only genes with $|\log2FC| \geq 0.4$ and Qvalue ≤ 0.05 were considered. PCA analysis, hierarchical clustering, functional annotation analysis (KEGG pathway, GO_C, GO_P) were performed in Dr. TOM platform of BGI. Dot plots showing the distribution of activation, differentiation and quiescence signature genes were generated in ggplot2 in R. The BAM files, TPM values will be uploaded to GEO database after acceptance of the manuscript.

Acknowledgement: We thank Dr. Kimberly Bowles at Life Science Core Facility of UT Arlington for the assistance in cell sorting experiments.

Funding: JZ was supported by grants from NIH (R01NS105621) and the Department of Defense AL170061(W81XWH1810684).

Figures and figure legends

Figure 1

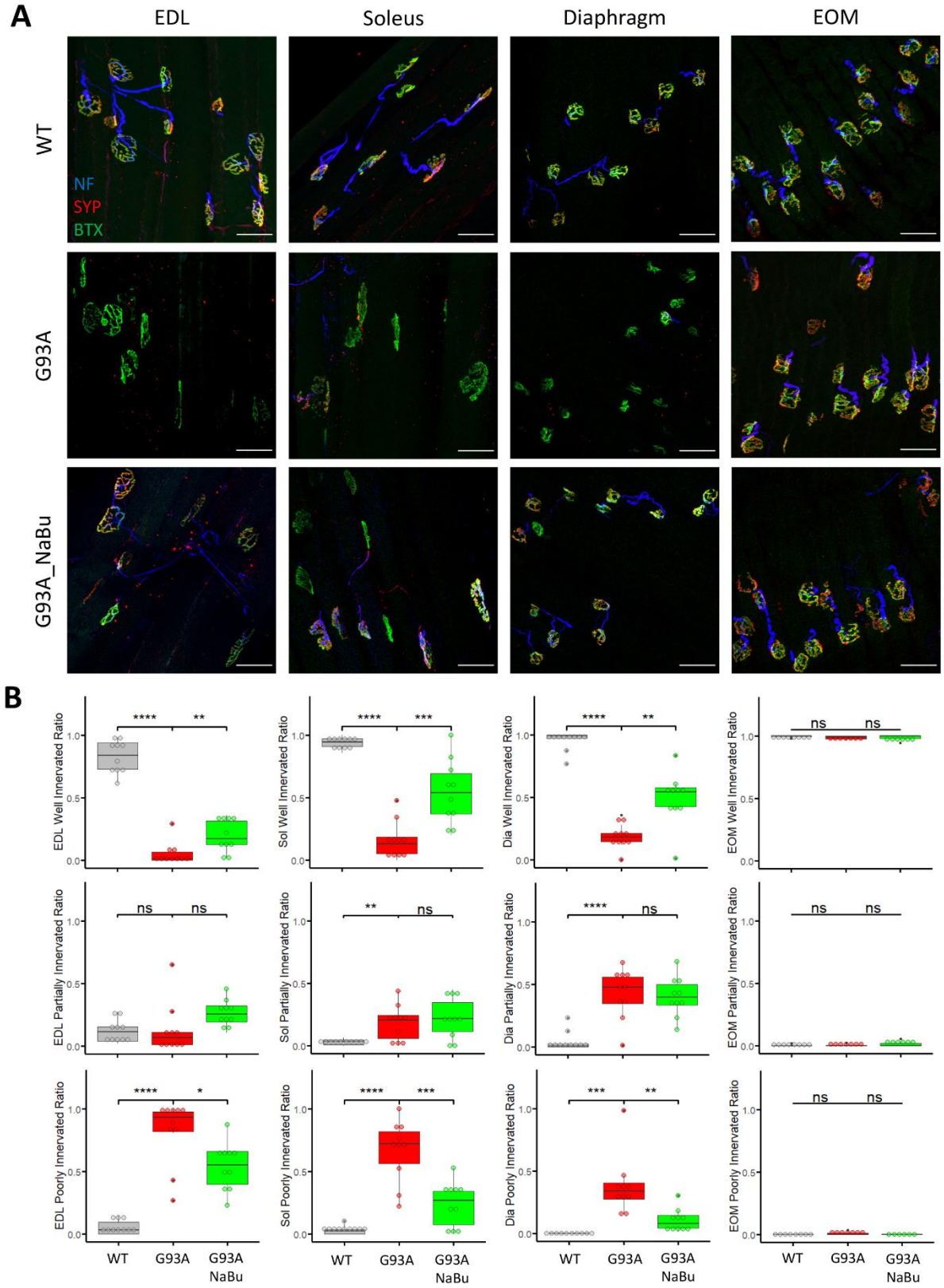

Figure 1. Characterizing NMJ integrity in muscles dissected from wildtype controls and end-stage G93A mice with or without NaBu feeding. (**A**) Representative compacted z-stack scan images of whole-mount EDL, soleus diaphragm extraocular muscles stained with antibodies against neurofilament medium chain (NF, labeling axons), synaptophysin (SYP, labeling axon terminals) and Alexa Fluor 488 conjugated α-Bungarotoxin (BTX, labeling AChRs on muscle membrane). scale bars, 50 μm. **(B)** Mean ratios of well innervated NMJs (SYP signals are present in >60% of BTX positive area), partially innervated NMJs (SYP signals are present in 30-60% of BTX positive area) and poorly innervated NMJs (SYP signals are present in <30% of BTX positive area) and in different types of muscles dissected from WT controls and end-stage G93A mice with or without NaBu feeding (tens to hundreds of NMJs were measured per muscle type per mice, also see Figure 1-figure supplement 1 and Figure 1-table supplement 1). * $P < 0.05$; ** $P < 0.01$; **** $P < 0.0001$; ns, not significant.

Figure 2

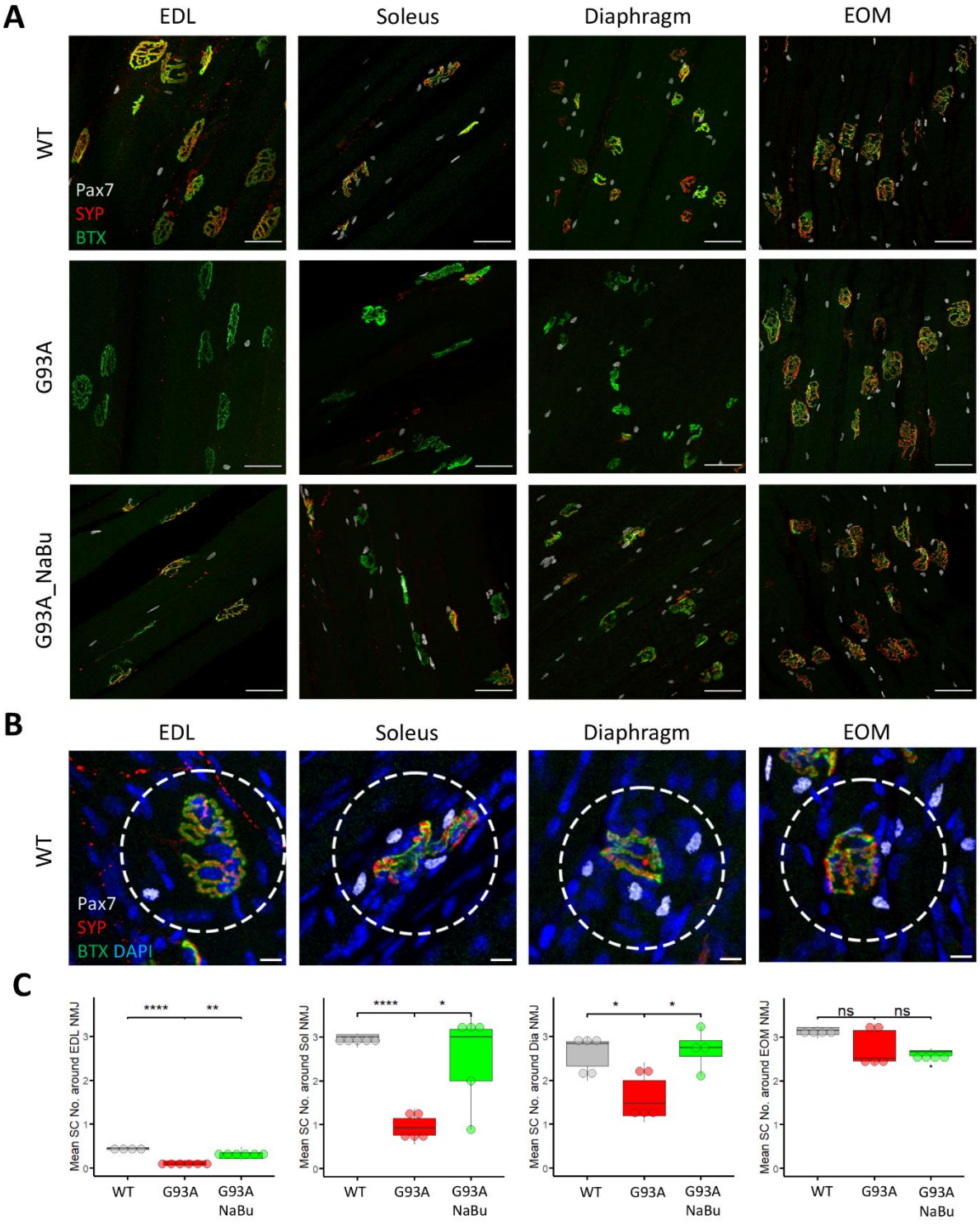
A
EDL
Soleus
Diaphragm
EOM
WT
G93A
G93A_NaBu
Pax7
SYP
BTX
B
EDL
Soleus
Diaphragm
EOM
WT
Pax7
SYP
BTX DAPI
C
Mean SC No. around EDL NMJ
Mean SC No. around Sol NMJ
Mean SC No. around Dia NMJ
Mean SC No. around EOM NMJ
****
**
*
ns
WT
G93A
G93A NaBu

Figure 2. Characterizing peri-NMJ SC abundance in muscles dissected from wildtype controls and end-stage G93A mice with or without NaBu feeding. (**A**) Representative compacted z-stack scan images of whole-mount EDL, soleus diaphragm extraocular muscles stained with antibodies against Pax7 (labeling SCs), SYP and BTX-Alexa Fluor 488. scale bars, 50 μm. To measure the abundance of SCs around NMJs, circles of 75 μm diameter were drawn around the NMJs and the number of nuclear $Pax7^{+}$ cells (co-localized with DAPI) were counted as shown in (**B**). Scale bars, 10 μm. (**C**) Mean number of SCs around NMJs in different types of muscles dissected from wildtype controls and end-stage G93A mice with or without NaBu feeding (tens to hundreds of NMJs were measured per muscle type per mice, see Figure 2-table supplement 1). * $P < 0.05$; ** $P < 0.01$; **** $P < 0.0001$; ns, not significant.

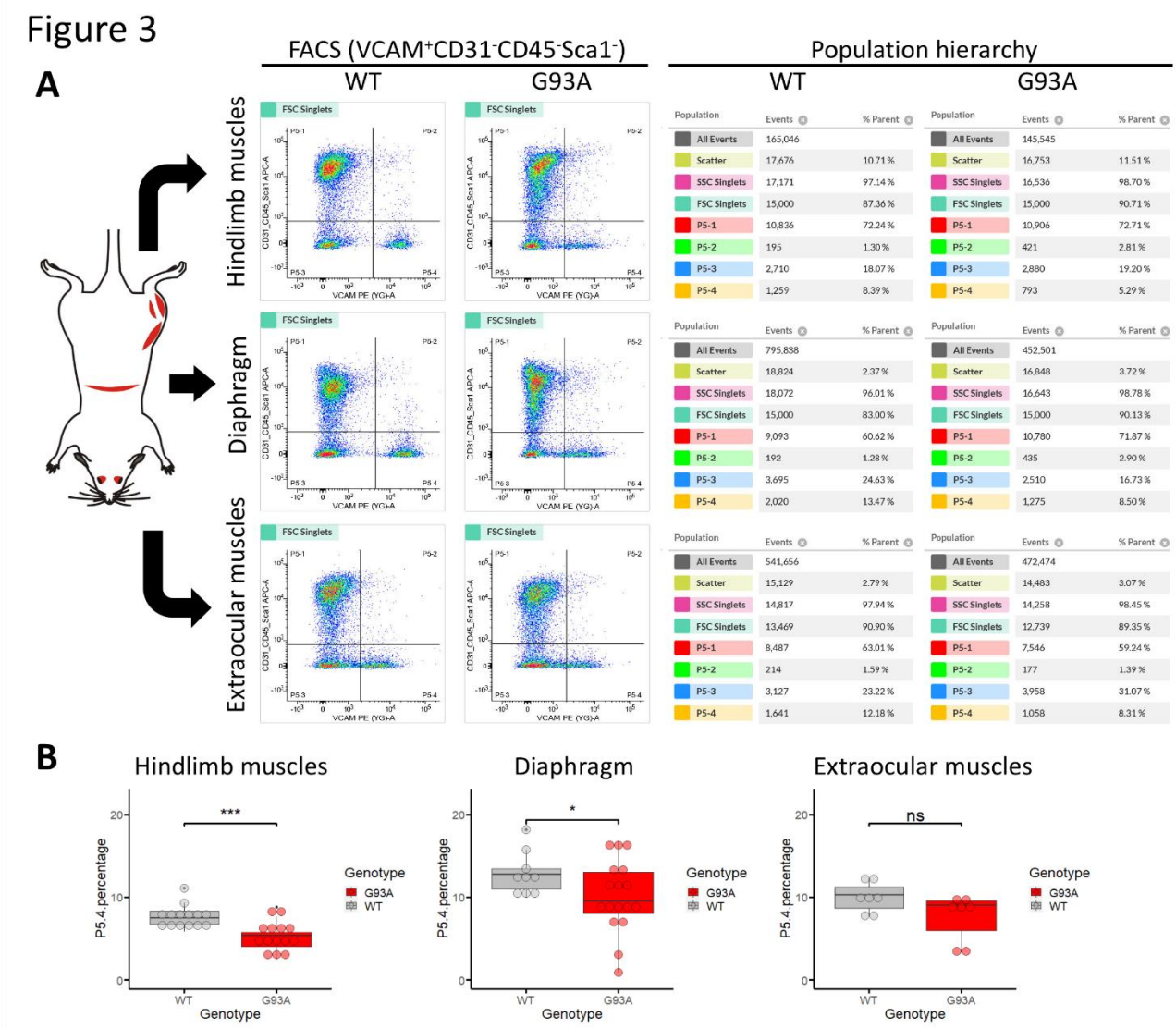

Figure 3. Isolation of SCs from wildtype and G93A muscles using fluorescence activated cell sorting. (**A**) Representative FACS profiles during the isolation of VCAM^{+}CD31^{-}CD45^{-}Sca1^{-} cells (gate P5-4). The corresponding population hierarchies are shown right to the plots. For single antibody staining controls, unstained controls and viability test, see Figure 3-figure supplement 1 and Figure 3-figure supplement 2. (**B**) Comparing the percentage of events in the P5-4 gate between cells isolated from WT and G93A mice. * $P < 0.05$; *** $P < 0.001$; ns: not significant.

Figure 4

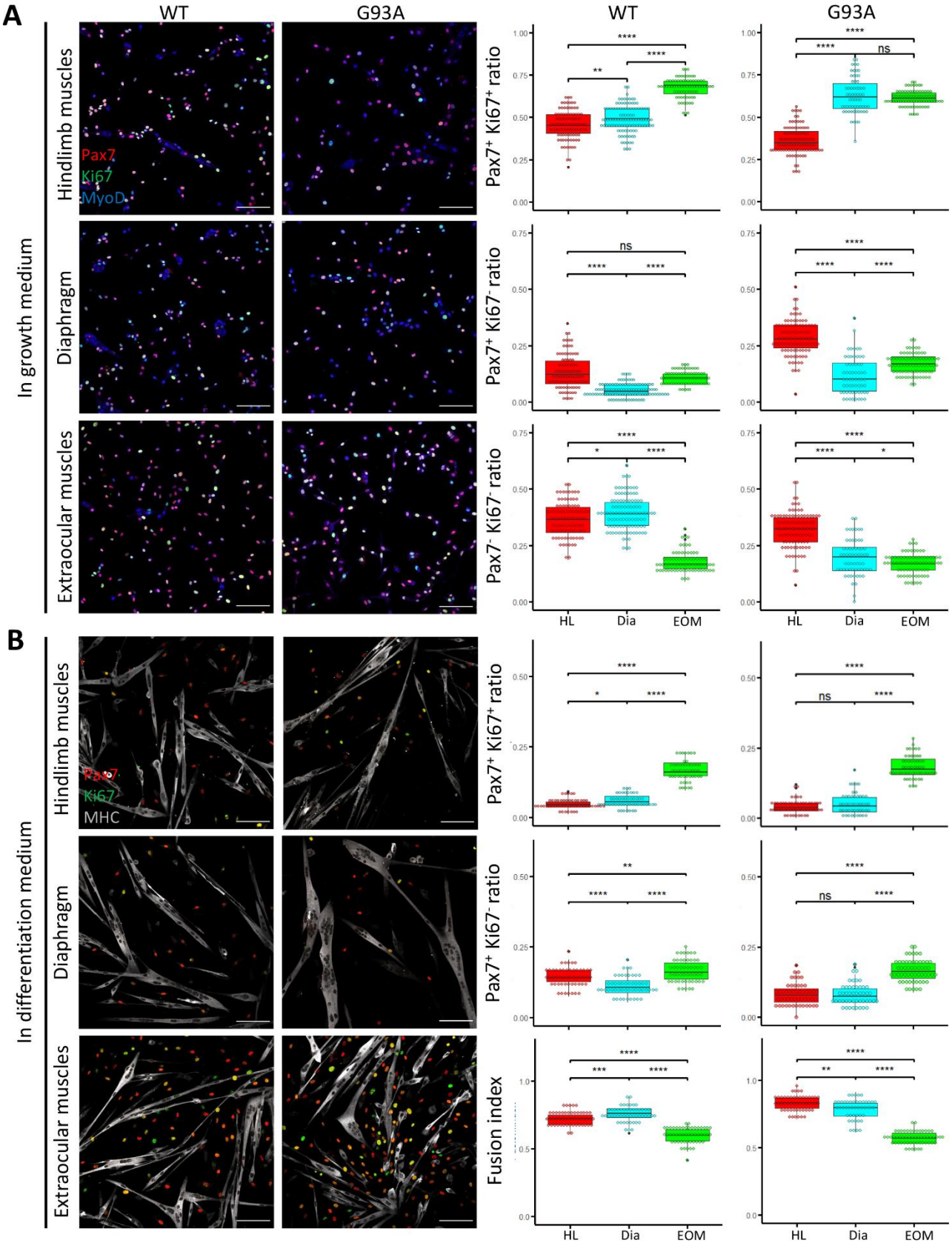
A
WT
G93A
WT
G93A
In growth medium
Hindlimb muscles
Diaphragm
Extraocular muscles
Pax7
Ki67
MyoD
Pax7+ Ki67+ ratio
Pax7+ Ki67- ratio
Pax7- Ki67- ratio
HL
Dia
EOM
B
In differentiation medium
Hindlimb muscles
Diaphragm
Extraocular muscles
Pax7
Ki67
MHC
Pax7+ Ki67+ ratio
Pax7+ Ki67- ratio
Fusion index
HL
Dia
EOM

Figure 4. Proliferation and differentiation properties of FACS-isolated SCs in culture. (**A**) Representative images of FACS-isolated SCs cultured for 4 days in growth medium stained with antibodies against Pax7, Ki67 (proliferating cell marker), MyoD (myogenic lineage marker). Measurement results for the ratios of $Pax7^{+}Ki67^{+}$, $Pax7^{+}Ki67^{-}$ and $Pax7^{-}Ki67^{-}$ cells are shown in the right two panels. Scale bars, 100 μm. * $P < 0.05$; ** $P < 0.01$; **** $P < 0.0001$; ns, not significant. (**B**) Representative images of FACS-isolated SCs cultured for 4 days in growth medium and 2 days in differentiation medium stained with antibodies against Pax7, Ki67, myosin heavy chain (MHC, differentiated myotube marker). Measurement results for the ratios of $Pax7^{+}Ki67^{+}$ and $Pax7^{+}Ki67^{-}$ cells, as well as the fusion indices are shown in the right two panels.

Figure 5

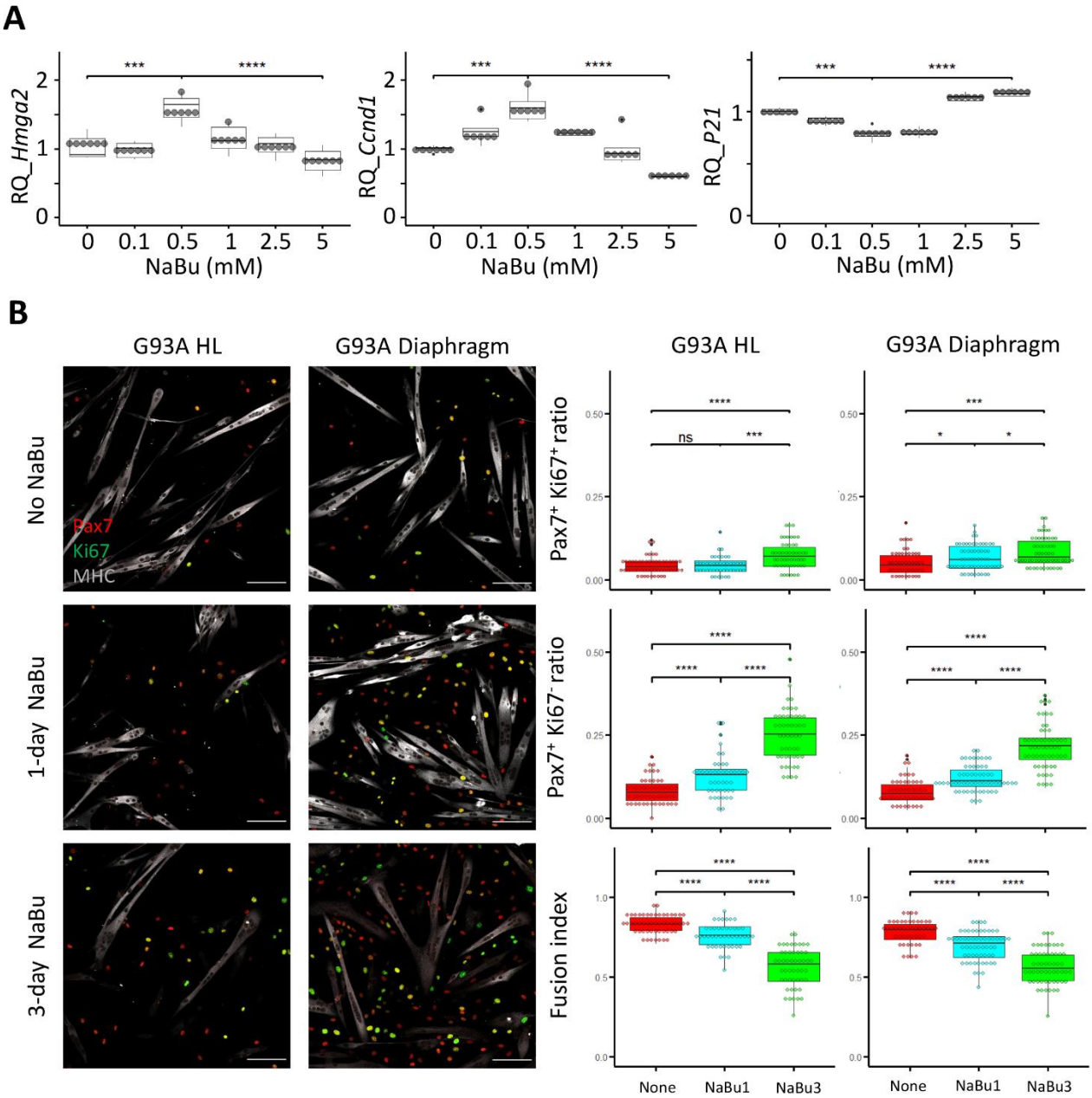

Figure 5. Proliferation and differentiation properties of FACS-isolated SCs with different NaBu treatment conditions. (**A**) qRT-PCR based relative quantification of *Hmga2*, *Ccnd1* and *P21* expression in FACS-isolated G93A HL SCs cultured with different doses of NaBu in growth medium for 1 day (n = 6). *** P < 0.001; **** P < 0.0001. (**B**) Left two panels show the representative images of FACS-isolated G93A HL and diaphragm SCs cultured in growth medium for 4 days and differentiation medium for 2 days and experienced different NaBu treatment conditions and stained with Pax7, Ki67 and MHC antibodies. Cells in top row were not treated with NaBu. Cells in the middle row were treated with NaBu for 1 day before the induction of differentiation (Day 4 of culture). Cells in the bottom row were treated with NaBu continuously for 3 days from the day before the induction of differentiation (Day 4-6 of culture). Scale bars, 100 μm. Measurement results for the ratios of $Pax7^{+}Ki67^{+}$ and $Pax7^{+}Ki67^{-}$ cells, as well as the fusion indices are shown in the right two panels. * P < 0.05; ns, not significant.

Figure 6

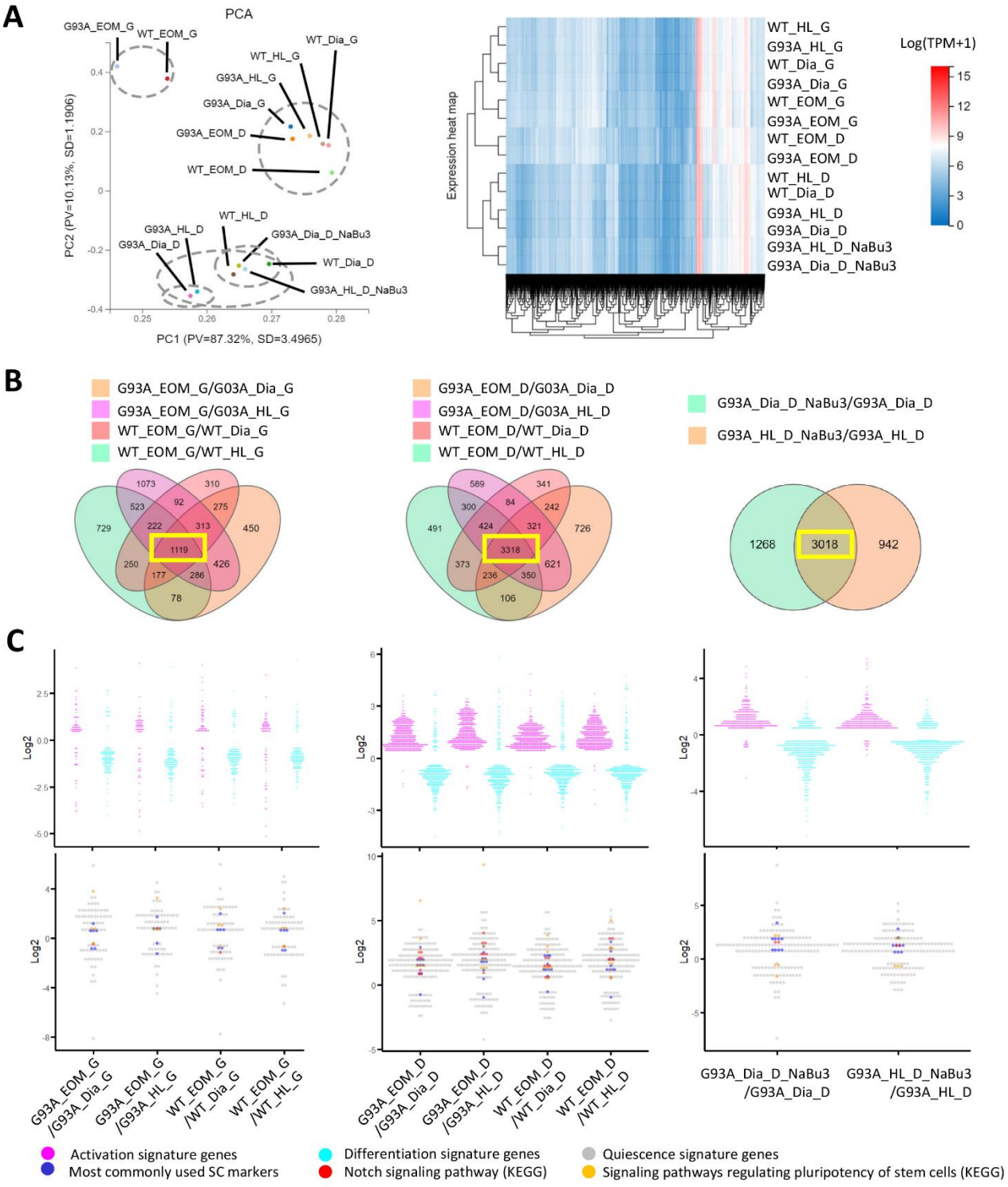
A
PCA
G93A_EOM_G
WT_EOM_G
WT_Dia_G
WT_HL_G
G93A_HL_G
G93A_Dia_G
G93A_EOM_D
WT_EOM_D
WT_HL_D
G93A_HL_D
G93A_Dia_D
G93A_Dia_D_NaBu3
WT_Dia_D
G93A_HL_D_NaBu3
PC2 (PV=10.13%, SD=1.1906)
PC1 (PV=87.32%, SD=3.4965)
Expression heat map
Log(TPM+1)
B
G93A_EOM_G/G03A_Dia_G
G93A_EOM_G/G03A_HL_G
WT_EOM_G/WT_Dia_G
WT_EOM_G/WT_HL_G
G93A_EOM_D/G03A_Dia_D
G93A_EOM_D/G03A_HL_D
WT_EOM_D/WT_Dia_D
WT_EOM_D/WT_HL_D
G93A_Dia_D_NaBu3/G93A_Dia_D
G93A_HL_D_NaBu3/G93A_HL_D
1268
3018
942
C
Log2
G93A_EOM_G /G93A_Dia_G
G93A_EOM_G /G93A_HL_G
WT_EOM_G /WT_Dia_G
WT_EOM_G /WT_HL_G
G93A_EOM_D /G93A_Dia_D
G93A_EOM_D /G93A_HL_D
WT_EOM_D /WT_Dia_D
WT_EOM_D /WT_HL_D
G93A_Dia_D_NaBu3 /G93A_Dia_D
G93A_HL_D_NaBu3 /G93A_HL_D
Activation signature genes
Most commonly used SC markers
Differentiation signature genes
Notch signaling pathway (KEGG)
Quiescence signature genes
Signaling pathways regulating pluripotency of stem cells (KEGG)

Figure 6. Comparing the transcriptomic profile and homeostasis preferences of SCs from different muscle origins cultured in growth and differentiation medium. (**A**) PCA analysis and hierarchical clustering results of different RNA-Seq samples. Samples with suffix “G” were SCs cultured in growth medium for 4 days. Suffix “D” denote SCs cultured in growth medium for 4 days and differentiation medium for 2 days. Suffix “NaBu3” denote SCs treated with 0.5 mM NaBu continuously for 3 days (Day 4-6 of culture). Dashed-line circles in PCA plot highlight samples close to each other in distance. (**B**) We identify genes differentially expressed in EOM SCs compared to their diaphragm and HL counterparts cultured in growth medium (leftmost panel) and differentiation medium (middle panel) by screening for genes shared by the four DEG lists (gold, magenta, pink and green in color) shown in the Venn diagrams. All DEG lists were generated based on the standard of |log2FC|>= 0.4 and FDR<= 0.001. Yellow box highlights the shared genes. To identify NaBu treatment signature genes, we screened for genes shared by the two DEG lists (green and gold in color) shown in the rightmost Venn diagram. (**C**) Dot plots in the upper row show the Log2FC of activation signature genes (magenta) and differentiation signature genes (cyan) identified in the 1119, 3318 and 3018 genes highlighted in yellow boxes in (B). Dot plots in the lower row show the Log2 FC of quiescence signature genes identified in the yellow-box highlighted genes in (B). Additionally, genes belonging to the following subgroups of quiescent signature genes: most commonly used SC markers, Notch signaling components and pluripotency signaling components are colored in dark blue, red and gold, respectively.

Figure 7

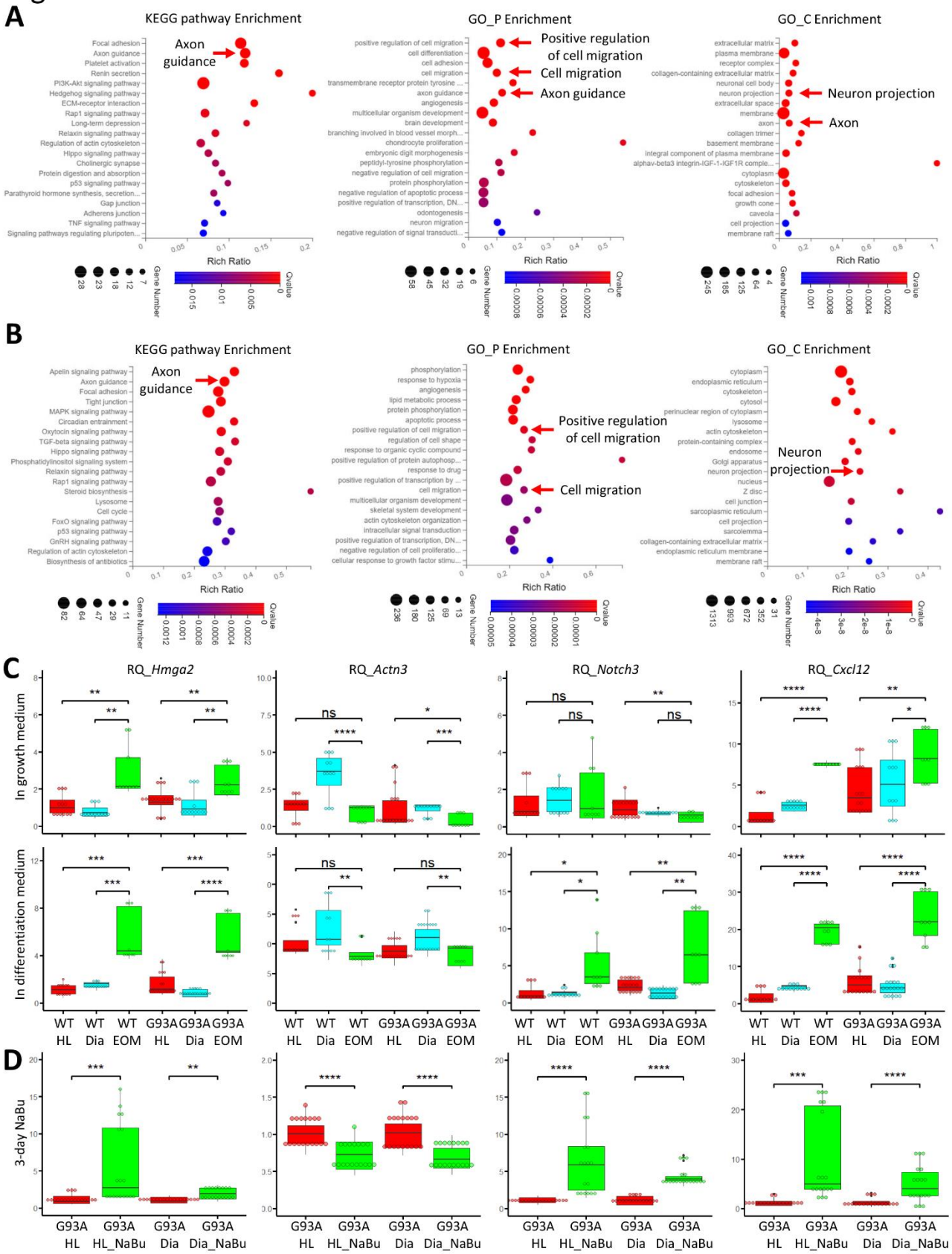
A
KEGG pathway Enrichment
Axon guidance
GO_P Enrichment
Positive regulation of cell migration
Cell migration
Axon guidance
GO_C Enrichment
Neuron projection
Axon
Rich Ratio
Gene Number
Qvalue
B
KEGG pathway Enrichment
Axon guidance
GO_P Enrichment
Positive regulation of cell migration
Cell migration
GO_C Enrichment
Neuron projection
C
RQ_Hmga2
RQ_Actn3
RQ_Notch3
RQ_Cxcl12
In growth medium
In differentiation medium
WT HL
WT Dia
WT EOM
G93A HL
G93A Dia
G93A EOM
D
3-day NaBu
G93A HL
G93A HL_NaBu
G93A Dia
G93A Dia_NaBu

Figure 7. Functional annotation analysis of EOM SC signature genes and NaBu treatment signature genes and qRT-PCR results. (**A**) Top KEGG pathway, GO_P and GO_C annotations of the 478 EOM signature genes (expressed higher in EOM SCs compared to diaphragm and HL counterparts cultured in both growth medium and differentiation medium). Arrows highlight annotations related to axon guidance and cell migration. (**B**) Top KEGG pathway, GO_P and GO_C annotations of the 3018 NaBu treatment signature genes shown in Figure 6B, rightmost panel. (**C**) qRT-PCR based relative quantification of *Hmga2* (activation signature gene), *Actn3* (differentiation signature gene), *Notch3* (quiescence signature gene) and *Cxcl12* (axon guidance molecule) expression in HL, diaphragm and EOM SCs cultured in growth and differentiation medium, respectively. * $P < 0.05$; ** $P < 0.01$; *** $P < 0.001$; **** $P < 0.0001$; ns, not significant. RNA samples were collected from 3-6 rounds of sorting and sorted cells were split into 3 replicates. (**D**) qRT-PCR based relative quantification of *Hmga2*, *Actn3*, *Notch3* and *Cxcl12* expression in G93A HL and diaphragm SCs with or without the 3-day NaBu treatment. RNA samples were collected from 6 rounds of sorting and sorted cells were split into 3 replicates.

Figure 8

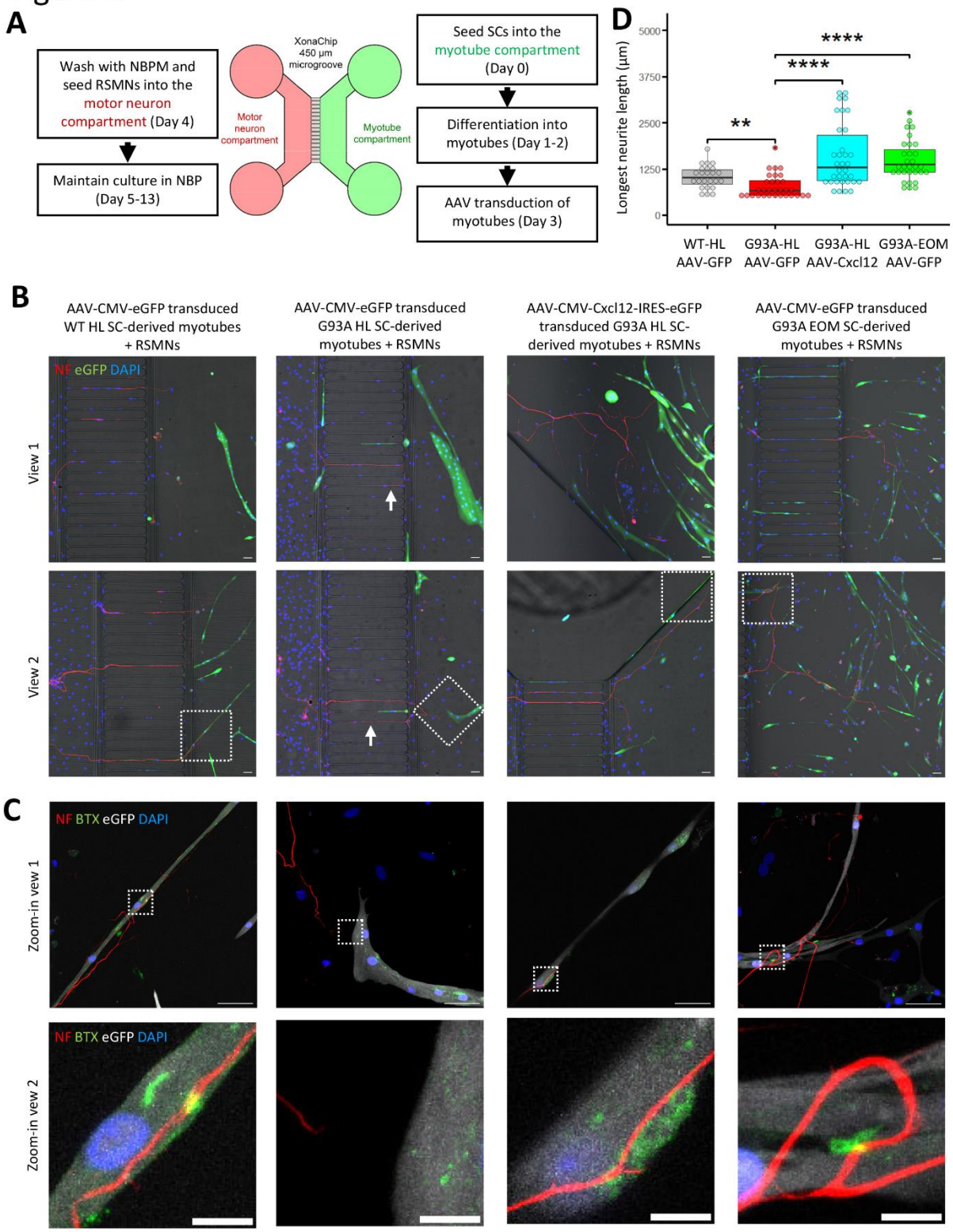
A
Wash with NBPM and seed RSMNs into the motor neuron compartment (Day 4)
Maintain culture in NBP (Day 5-13)
XonaChip 450 µm microgroove
Motor neuron compartment
Myotube compartment
Seed SCs into the myotube compartment (Day 0)
Differentiation into myotubes (Day 1-2)
AAV transduction of myotubes (Day 3)
D
Longest neurite length (µm)
5000
3750
2500
1250
0
**
****
****
WT-HL AAV-GFP
G93A-HL AAV-GFP
G93A-HL AAV-Cxcl12
G93A-EOM AAV-GFP
B
AAV-CMV-eGFP transduced WT HL SC-derived myotubes + RSMNs
AAV-CMV-eGFP transduced G93A HL SC-derived myotubes + RSMNs
AAV-CMV-Cxcl12-IRES-eGFP transduced G93A HL SC-derived myotubes + RSMNs
AAV-CMV-eGFP transduced G93A EOM SC-derived myotubes + RSMNs
View 1
View 2
NF eGFP DAPI
C
Zoom-in vew 1
Zoom-in vew 2
NF BTX eGFP DAPI

Figure 8. Coculture of AAV transduced SC derived myotubes with rat spinal motor neurons in compartmentalized microfluidic chambers. (A) Schematic representation of XonaChip spatial configuration and coculture experiment timeline. NBPM: Neurobasal Plus Medium; RSMNs: rat spinal motor neurons. **(B)** Representative composite images of RSMNs cocultured with: 1. WT HL SC-derived myotubes transduced with AAV-CMV-eGFP; 2. G93A HL SC-derived myotubes transduced with AAV-CMV-eGFP; 3. G93A HL SC-derived myotubes transduced with AAV-CMV-Cxcl12-IRES-eGFP; 4. G93A EOM SC-derived myotubes transduced with AAV-CMV-eGFP. Arrows highlight RSMN neurites crossed the microgrooves but stayed close to the edges and grew backward. Also see Figure 8-figure supplement 2A. Boxed regions are enlarged below. Scale bars: 50 μm. **(C)** Zoom-in views of RSMN neurites innervated or missed the AChR clusters (BTX positive patches). Boxed regions are further enlarged below. Scale bars: 50 μm, 10 μm. **(D)** Measured lengths of the longest neurites derived from RSMN cells (presumably axons) crossing the 450 μm microgrooves. n = 24, 31, 34,31 cells for the 4 groups, respectively (from 3 rounds of coculture experiments).

Figure 9

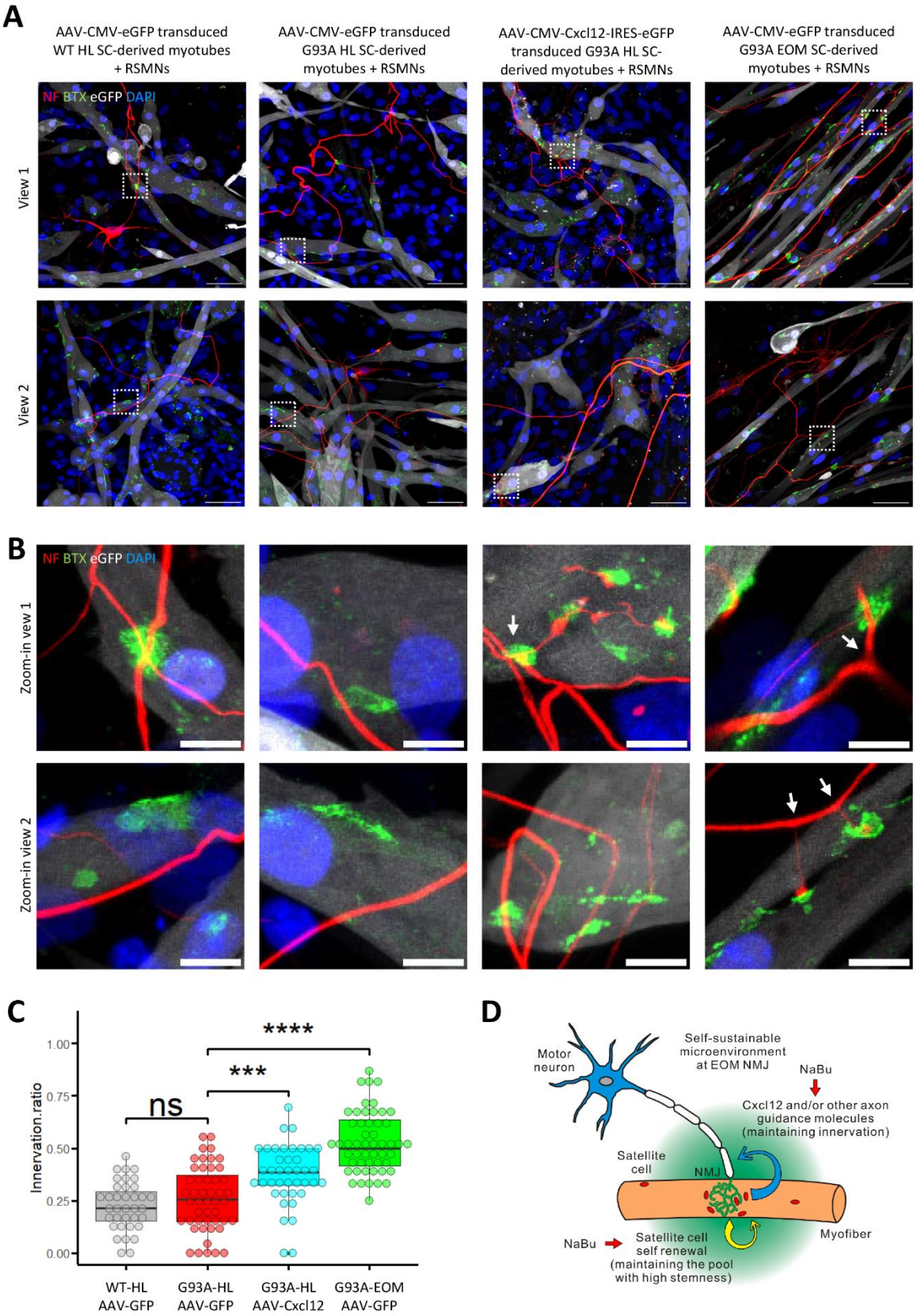
A
AAV-CMV-eGFP transduced WT HL SC-derived myotubes + RSMNs
AAV-CMV-eGFP transduced G93A HL SC-derived myotubes + RSMNs
AAV-CMV-Cxcl12-IRES-eGFP transduced G93A HL SC-derived myotubes + RSMNs
AAV-CMV-eGFP transduced G93A EOM SC-derived myotubes + RSMNs
NF BTX eGFP DAPI
View 1
View 2
B
Zoom-in vew 1
Zoom-in view 2
C
Innervation.ratio
1.00
0.75
0.50
0.25
0.00
ns
***
****
WT-HL AAV-GFP
G93A-HL AAV-GFP
G93A-HL AAV-Cxcl12
G93A-EOM AAV-GFP
D
Motor neuron
Self-sustainable microenvironment at EOM NMJ
NaBu
Cxcl12 and/or other axon guidance molecules (maintaining innervation)
Satellite cell
NMJ
Myofiber
NaBu
Satellite cell self renewal (maintaining the pool with high stemness)

Figure 9. Coculture of AAV transduced SC derived myotubes with rat spinal motor neurons within the same compartment. (A) Representative composite images of RSMNs cocultured with: 1. WT HL SC-derived myotubes transduced with AAV-CMV-eGFP; 2. G93A HL SC-derived myotubes transduced with AAV-CMV-eGFP; 3. G93A HL SC-derived myotubes transduced with AAV-CMV-Cxcl12-IRES-eGFP; 4. G93A EOM SC-derived myotubes transduced with AAV-CMV-eGFP. The timeline was the same as that in Figure 8 but RSMNs were seeded on top of myotubes. Boxed regions are enlarged in (B). Scale bars: 50 μm. **(B)** Zoom-in views of innervated and non-innervated AChR clusters on myotubes having contact with RSMN neurites. Arrows highlight branching phenomena observed in RSMN neurites innervating AChR clusters. Scale bars: 10 μm. **(C)** Quantification of innervation ratios of AChR clusters (area > 10 μm^2) in myotubes in contact with RSMN neurites. n = 37, 48, 40, 52 z-stack images for the 4 groups, respectively (from 3 rounds of coculture experiments). Also see methods for detailed description. *** $P < 0.001$; **** $P < 0.0001$; ns, not significant. **(D)** Graphic summary of the potential mechanisms contributing to EOM NMJ integrity maintenance during ALS progression mimicked by NaBu treatment.

Legends for supplementary figures and tables

Figure 1-figure supplement 1. Representative images of the three types of NMJs and qRT-PCR results of *Scn5a* expression in whole muscles. (**A**) Representative images of well-innervated, partially innervated and poorly innervated NMJs in WT diaphragm muscles. BTX: Alexa Fluor 488 conjugated α-Bungarotoxin; SYP: synaptophysin; NF: neurofilament medium chain. (**B**) qRT-PCR based relative quantification of *Scn5a* expression using RNAs extracted from whole muscles of EDL, soleus, diaphragm and EOM. * $P < 0.05$; ** $P < 0.01$; ns, not significant.

Figure 1-table supplement 1. Quantification results of the three types of NMJs in muscles of different origins and treatment conditions.

Figure 1-table supplement 2. qRT-PCR results for *Scn5a* relative expression in whole muscles of different origins and treatment conditions

Figure 2-table supplement 1. Quantification results of averaged peri-NMJ SC numbers in muscles of different origins and treatment conditions.

Figure 3-figure supplement 1. Representative FACS profiles of single antibody staining controls. (**A**) FACS profile of cells isolated from WT HL muscles and stained only with PE conjugated anti-mouse Vcam1 antibody at 600 ng/10^6 cells. FSC-H/SSC-H, FSC-A/SSC-A, SSC-H/SSC-W, FSC-H/FSC-W, Time/FSC-H, Vcam1/CD31_CD45_Sca-1 plots, CD31_CD45_Sca-1 count histogram and Vcam1 count histogram are shown on the left. Population hierarchies were shown on the right. (**B**) FACS profile of cells stained only with APC conjugated anti-mouse CD31 antibody at 400 ng/10^6 cells. (**C**) FACS profile of cells stained only with APC conjugated anti-mouse CD45 antibody at 400 ng/10^6 cells. (**D**) FACS profile of cells stained only with APC conjugated anti-mouse Sca-1 antibody at 200 ng/10^6 cells.

Figure 3-figure supplement 2. Viability assessment of cells for sorting using methyl green. (**A**) FACS profile of unstained cells isolated from WT HL muscles. FSC-H/SSC-H, FSC-A/SSC-A, SSC-H/SSC-W, FSC-H/FSC-W, Vcam1/Methyl green, Time/FSC-H plots, Methyl green count histogram and Vcam1 count histogram are shown on the left. Population hierarchies were shown on the right. (**B**) FACS profile of methyl green stained cells with 50% dead cells (through methanol dehydration) spiked in. (**C**) FACS profile of methyl green stained cells without any spiked-in dead cells. (**D**) FACS profile of methyl green and Vcam1 double-stained cells (no dead cells spiked in).

Figure 3-table supplement 1. Percentage of P5-4 events recorded in different rounds of sorting.

Figure 4-figure supplement 1. Comparing proliferation and differentiation properties of cultured SCs from WT and G93A muscles. (**A**) Comparing the ratios of $Pax7^+Ki67^+$, $Pax7^+Ki67^-$ and $Pax7^-Ki67^-$ cells in the SCs cultured in growth medium, respectively. **** $P < 0.0001$; *** $P < 0.001$; ns, not significant. (**B**) Comparing the ratios of $Pax7^+Ki67^+$, $Pax7^+Ki67^-$ cells and fusion indices of the SCs cultured in differentiation medium, respectively. **** $P < 0.0001$; *** $P < 0.001$; * $P < 0.05$; ns, not significant.

Figure 6-figure supplement 1. Compiling the activation signature gene and differentiation signature gene lists. (**A**) Hierarchical clustering results of WT and G93A SCs cultured in growth and differentiation medium. In both cases samples cultured in the same medium condition are clustered together. (**B**) Bar chart on the left shows differentially expressed genes between SCs cultured in growth and differentiation medium, with SCs derived from WT and G93A mice analyzed separately. The Venn diagram highlights 2536 of these genes shared between WT and G93A SCs. 1187 of them expressed higher in SCs in growth medium are considered activation signature genes. The rest 1349 genes expressed higher in SCs in differentiation medium are considered differentiation signature genes.

Functional annotation analysis below highlights top KEGG pathways, gene ontology_biological processes and gene ontology_cellular components enriched in these two lists of genes, respectively.

Figure 6-table supplement 1. Three subgroups of quiescent signature genes identified in the DEG lists comparing EOM SCs to diaphragm and HL counterparts cultured in differentiation medium. Log2FC and FDR are shown and genes are ranked according to relative abundance (TPM, from highest to lowest) in wildtype EOM SCs.

Figure 6-table supplement 2. Three subgroups of quiescent signature genes identified in the DEG lists comparing EOM SCs to diaphragm and HL counterparts cultured in growth medium. Log2FC and FDR are shown and genes are ranked according to relative abundance (TPM, from highest to lowest) in wildtype EOM SCs.

Figure 6-table supplement 3. Three subgroups of quiescent signature genes identified in the DEG lists comparing G93A diaphragm and HL SCs with and without 3-day NaBu treatment. Log2FC and FDR are shown and genes are ranked according to relative abundance (TPM, from highest to lowest) in G93A diaphragm SCs.

Figure 7-figure supplement 1. Top functional annotations of EOM SC signature genes cultured in growth medium and differentiation medium. (A) Top KEGG pathway, GO_P and GO_C annotations of the 621 DEGs more abundant in EOM SCs compared to diaphragm and HL counterparts cultured in growth medium. **(B)** Top KEGG pathway, GO_P and GO_C annotations of the 2424 DEGS more abundant in EOM SCs compared to diaphragm and HL counterparts cultured in differentiation medium.

Figure 7-table supplement 1. Axon guidance related genes (KEGG) identified in EOM SC signature genes cultured in growth medium. Log2FC and FDR are shown and genes are ranked according to relative abundance (TPM, from highest to lowest) in wildtype EOM SCs.

Figure 7-table supplement 2. Axon guidance related genes (KEGG) identified in EOM SC signature genes cultured in differentiation medium. Log2FC and FDR are shown and genes are ranked according to relative abundance (TPM, from highest to lowest) in wildtype EOM SCs.

Figure 7-table supplement 3. Axon guidance related genes (KEGG) identified in NaBu treatment signature genes. Log2FC and FDR are shown and genes are ranked according to relative abundance (TPM, from highest to lowest) in G93A HL SCs with 3-day NaBu treatment.

Figure 7-table supplement 4. qRT-PCR results for *Hmga2*, *Actn3*, *Notch3* and *Cxcl12* in SCs of different muscle origins cultured in growth medium.

Figure 7-table supplement 5. qRT-PCR results for *Hmga2*, *Actn3*, *Notch3* and *Cxcl12* in SCs of different muscle origins cultured in differentiation medium.

Figure 7-table supplement 6. qRT-PCR results for *Hmga2*, *Actn3*, *Notch3* and *Cxcl12* in G93A diaphragm and HL SCs with or without 3-day NaBu treatment.

Figure 8-figure supplement 1. Representative views of AAV transduced G93A HL SC derived myotubes stained with Cxcl12 and eGFP antibodies. (A) G93A HL SC derived myotubes transduced with AAV8-CMV-eGFP and stained with Cxcl12 and GFP antibodies. **(B)** G93A HL SC derived from myotubes transduced with AAV8-CMV-Cxcl12-IRES-eGFP and stained with Cxcl12 and GFP antibodies. Boxed regions are enlarged on the right and staining patterns of individual antibody are shown below (DAPI counterstaining highlights nucleus). Scale bars: 50 μm, 10 μm (enlarged images).

Figure 8-figure supplement 2. Additional representative views of neuromuscular coculture in compartmentalized microfluidic chamber. (A) Cocultures of RSMNs with G93A HL SC derived myotubes transduced with AAV8-CMV-eGFP. Boxed regions are enlarged below. Arrows highlight the RSMN axons turning back towards the neuronal compartment after crossing the 450 µm microgrooves. Scale bars: 50 µm. **(B)** Cocultures of RSMNs with G93A HL SC derived myotubes transduced with AAV8-CMV-Cxcl12-IRES-eGFP. Boxed regions are enlarged below to highlight neurites entangling myotubes located close to the microgrooves. Scale bars: 50 µm.

Figure 9-figure supplement 1. Additional representative views of neuromuscular coculture within the same compartment. (A) Cocultures of RSMNs with WT HL SC derived myotubes transduced with AAV8-CMV-eGFP. Boxed regions are enlarged on the right to highlight innervated and non-innervated AChR clusters. Scale bars: 50 µm, 10 µm (enlarged images). **(B)** Cocultures of RSMNs with G93A HL SC derived myotubes transduced with AAV8-CMV-eGFP. **(C)** Cocultures of RSMNs with G93A HL SC derived myotubes transduced with AAV8-CMV-Cxcl12-IRES-eGFP. **(D)** Cocultures of RSMNs with G93A EOM SC derived myotubes transduced with AAV8-CMV-eGFP. Boxed regions are enlarged on the right to highlight innervated AChR clusters located on the same individual G93A EOM-SC derived myotube.

References

1. Vucic, S.; Rothstein, J.D.; Kiernan, M.C. Advances in treating amyotrophic lateral sclerosis: insights from pathophysiological studies. *Trends in neurosciences* **2014**, *37*, 433-442.
2. Domellöf, F.P. The Extraocular Muscles Are Selectively Spared in ALS. In *Amyotrophic Lateral Sclerosis-Recent Advances and Therapeutic Challenges*; IntechOpen: 2019.
3. Nijssen, J.; Comley, L.H.; Hedlund, E. Motor neuron vulnerability and resistance in amyotrophic lateral sclerosis. *Acta neuropathologica* **2017**, *133*, 863-885.
4. Zimmermann, L.; Morado-Díaz, C.J.; de Carrizosa, M.A.D.-L.; Rosa, R.; May, P.J.; Streicher, J.; Pastor, Á.M.; Blumer, R. Axons giving rise to the palisade endings of feline extraocular muscles display motor features. *Journal of Neuroscience* **2013**, *33*, 2784-2793.
5. Tjust, A.E.; Brännstrom, T.; Pedrosa Domellöf, F. Unaffected motor endplate occupancy in eye muscles of ALS G93A mouse model. *Frontiers in bioscience (Scholar edition)* **2012**, *4*, 1547-1555.
6. Ahmadi, M.; Liu, J.-X.; Brännström, T.; Andersen, P.M.; Stål, P.; Pedrosa-Domellöf, F. Human extraocular muscles in ALS. *Investigative ophthalmology & visual science* **2010**, *51*, 3494-3501.
7. Valdez, G.; Tapia, J.C.; Lichtman, J.W.; Fox, M.A.; Sanes, J.R. Shared resistance to aging and ALS in neuromuscular junctions of specific muscles. *PloS one* **2012**, *7*, e34640.
8. Alexianu, M.E.; Ho, B.K.; Mohamed, A.H.; La Bella, V.; Smith, R.G.; Appel, S.H. The role of calcium-binding proteins in selective motoneuron vulnerability in amyotrophic lateral sclerosis. *Annals of Neurology: Official Journal of the American Neurological Association and the Child Neurology Society* **1994**, *36*, 846-858.
9. Ince, P.; Stout, N.; Shaw, P.; Slade, J.; Hunziker, W.; Heizmann, C.; Baimbridge, K. Parvalbumin and calbindin D-28k in the human motor system and in motor neuron disease. *Neuropathology and applied neurobiology* **1993**, *19*, 291-299.
10. Mosier, D.R.; Siklós, L.; Appel, S.H. Resistance of extraocular motoneuron terminals to effects of amyotrophic lateral sclerosis sera. *Neurology* **2000**, *54*, 252-252.
11. Clement, A.; Nguyen, M.; Roberts, E.; Garcia, M.; Boillee, S.; Rule, M.; McMahon, A.; Doucette, W.; Siwek, D.; Ferrante, R. Wild-type nonneuronal cells extend survival of SOD1 mutant motor neurons in ALS mice. *science* **2003**, *302*, 113-117.

12. Di Giorgio, F.P.; Carrasco, M.A.; Siao, M.C.; Maniatis, T.; Eggan, K. Non–cell autonomous effect of glia on motor neurons in an embryonic stem cell–based ALS model. *Nature neuroscience* **2007**, *10*, 608-614.
13. Nagai, M.; Re, D.B.; Nagata, T.; Chalazonitis, A.; Jessell, T.M.; Wichterle, H.; Przedborski, S. Astrocytes expressing ALS-linked mutated SOD1 release factors selectively toxic to motor neurons. *Nature neuroscience* **2007**, *10*, 615-622.
14. Marchetto, M.C.; Muotri, A.R.; Mu, Y.; Smith, A.M.; Cezar, G.G.; Gage, F.H. Non-cell-autonomous effect of human SOD1G37R astrocytes on motor neurons derived from human embryonic stem cells. *Cell stem cell* **2008**, *3*, 649-657.
15. Yamanaka, K.; Chun, S.J.; Boillee, S.; Fujimori-Tonou, N.; Yamashita, H.; Gutmann, D.H.; Takahashi, R.; Misawa, H.; Cleveland, D.W. Astrocytes as determinants of disease progression in inherited ALS.
16. Meyer, K.; Ferraiuolo, L.; Miranda, C.J.; Likhite, S.; McElroy, S.; Renusch, S.; Ditsworth, D.; Lagier-Tourenne, C.; Smith, R.A.; Ravits, J. Direct conversion of patient fibroblasts demonstrates non-cell autonomous toxicity of astrocytes to motor neurons in familial and sporadic ALS. *Proceedings of the National Academy of Sciences* **2014**, *111*, 829-832.
17. Wong, M.; Martin, L.J. Skeletal muscle-restricted expression of human SOD1 causes motor neuron degeneration in transgenic mice. *Human molecular genetics* **2010**, *19*, 2284-2302.
18. Fischer, L.R.; Culver, D.G.; Tennant, P.; Davis, A.A.; Wang, M.; Castellano-Sanchez, A.; Khan, J.; Polak, M.A.; Glass, J.D. Amyotrophic lateral sclerosis is a distal axonopathy: evidence in mice and man. *Experimental neurology* **2004**, *185*, 232-240.
19. Dobrowolny, G.; Giacinti, C.; Pelosi, L.; Nicoletti, C.; Winn, N.; Barberi, L.; Molinaro, M.; Rosenthal, N.; Musarò, A. Muscle expression of a local Igf-1 isoform protects motor neurons in an ALS mouse model. *The Journal of cell biology* **2005**, *168*, 193-199.
20. Harandi, V.M.; Lindquist, S.; Kolan, S.S.; Brännström, T.; Liu, J.-X. Analysis of neurotrophic factors in limb and extraocular muscles of mouse model of amyotrophic lateral sclerosis. *PLoS One* **2014**, *9*, e109833.
21. Harandi, V.M.; Gaied, A.R.; Brännström, T.; Domellöf, F.P.; Liu, J.-X. Unchanged neurotrophic factors and their receptors correlate with sparing in extraocular muscles in amyotrophic lateral sclerosis. *Investigative ophthalmology & visual science* **2016**, *57*, 6831-6842.
22. Liu, W.; Wei-LaPierre, L.; Klose, A.; Dirksen, R.T.; Chakkalakal, J.V. Inducible depletion of adult skeletal muscle stem cells impairs the regeneration of neuromuscular junctions. *elife* **2015**, *4*, e09221.
23. Liu, W.; Klose, A.; Forman, S.; Paris, N.D.; Wei-LaPierre, L.; Cortes-Lopez, M.; Tan, A.; Flaherty, M.; Miura, P.; Dirksen, R.T. Loss of adult skeletal muscle stem cells drives age-related neuromuscular junction degeneration. *Elife* **2017**, *6*, e26464.
24. Stuelsatz, P.; Shearer, A.; Li, Y.; Muir, L.A.; Ieronimakis, N.; Shen, Q.W.; Kirillova, I.; Yablonka-Reuveni, Z. Extraocular muscle satellite cells are high performance myo-engines retaining efficient regenerative capacity in dystrophin deficiency. *Developmental biology* **2015**, *397*, 31-44.
25. Davie, J.R. Inhibition of histone deacetylase activity by butyrate. *The Journal of nutrition* **2003**, *133*, 2485S-2493S.
26. Sincennes, M.-C.; Brun, C.E.; Rudnicki, M.A. Concise review: epigenetic regulation of myogenesis in health and disease. *Stem cells translational medicine* **2016**, *5*, 282-290.
27. Moresi, V.; Marroncelli, N.; Adamo, S. New insights into the epigenetic control of satellite cells. *World journal of stem cells* **2015**, *7*, 945.
28. Iezzi, S.; Cossu, G.; Nervi, C.; Sartorelli, V.; Puri, P.L. Stage-specific modulation of skeletal myogenesis by inhibitors of nuclear deacetylases. *Proceedings of the National Academy of Sciences* **2002**, *99*, 7757-7762.
29. Johnston, L.A.; Tapscott, S.; Eisen, H. Sodium butyrate inhibits myogenesis by interfering with the transcriptional activation function of MyoD and myogenin. *Molecular and cellular biology* **1992**, *12*, 5123-5130.

30. Zhang, Y.-g.; Wu, S.; Yi, J.; Xia, Y.; Jin, D.; Zhou, J.; Sun, J. Target intestinal microbiota to alleviate disease progression in amyotrophic lateral sclerosis. *Clinical therapeutics* **2017**, *39*, 322-336.
31. Xiao, Y.; Karam, C.; Yi, J.; Zhang, L.; Li, X.; Yoon, D.; Wang, H.; Dhakal, K.; Ramlow, P.; Yu, T. ROS-related mitochondrial dysfunction in skeletal muscle of an ALS mouse model during the disease progression. *Pharmacological research* **2018**, *138*, 25-36.
32. Li, A.; Li, X.; Yi, J.; Ma, J.; Zhou, J. Butyrate Feeding Reverses CypD-Related Mitoflash Phenotypes in Mouse Myofibers. *International journal of molecular sciences* **2021**, *22*, 7412.
33. Li, X.; Dong, L.; Li, A.; Yi, J.; Brotto, M.; Zhou, J. Butyrate ameliorates mitochondrial respiratory capacity of the motor-neuron-like cell line NSC34-G93A, a cellular model for ALS. *Biomolecules* **2022**, *12*, 333.
34. Sekiguchi, K.; Kanda, F.; Mitsui, S.; Kohara, N.; Chihara, K. Fibrillation potentials of denervated rat skeletal muscle are associated with expression of cardiac-type voltage-gated sodium channel isoform Nav1. 5. *Clinical neurophysiology* **2012**, *123*, 1650-1655.
35. Rowan, S.L.; Rygiel, K.; Purves-Smith, F.M.; Solbak, N.M.; Turnbull, D.M.; Hepple, R.T. Denervation causes fiber atrophy and myosin heavy chain co-expression in senescent skeletal muscle. *PloS one* **2012**, *7*, e29082.
36. Carreras, D.; Martinez-Moreno, R.; Pinsach-Abuin, M.l.; Santafe, M.M.; Gomà, P.; Brugada, R.; Scornik, F.S.; Pérez, G.J.; Pagans, S. Epigenetic changes governing Scn5a expression in denervated skeletal muscle. *International journal of molecular sciences* **2021**, *22*, 2755.
37. Liu, L.; Cheung, T.H.; Charville, G.W.; Rando, T.A. Isolation of skeletal muscle stem cells by fluorescence-activated cell sorting. *Nature protocols* **2015**, *10*, 1612-1624.
38. Metzger, J.M.; Scheidt, K.; Fitts, R.H. Histochemical and physiological characteristics of the rat diaphragm. *Journal of Applied Physiology* **1985**, *58*, 1085-1091.
39. Rochester, D.F. The diaphragm: contractile properties and fatigue. *The Journal of clinical investigation* **1985**, *75*, 1397-1402.
40. Polla, B.; D'antona, G.; Bottinelli, R.; Reggiani, C. Respiratory muscle fibres: specialisation and plasticity. *Thorax* **2004**, *59*, 808-817.
41. Augusto, V.; Padovani, C.R.; Campos, G.E.R. Skeletal muscle fiber types in C57BL6J mice. *Journal of Morphological Sciences* **2017**, *21*, 0-0.
42. Prieto, D.; Aparicio, G.; Morande, P.E.; Zolessi, F.R. A fast, low cost, and highly efficient fluorescent DNA labeling method using methyl green. *Histochemistry and cell biology* **2014**, *142*, 335-345.
43. Ancel, S.; Stuelsatz, P.; Feige, J.N. Muscle stem cell quiescence: controlling stemness by staying asleep. *Trends in Cell Biology* **2021**, *31*, 556-568.
44. Fukada, S.i.; Uezumi, A.; Ikemoto, M.; Masuda, S.; Segawa, M.; Tanimura, N.; Yamamoto, H.; Miyagoe-Suzuki, Y.; Takeda, S.i. Molecular signature of quiescent satellite cells in adult skeletal muscle. *Stem cells* **2007**, *25*, 2448-2459.
45. Fujimaki, S.; Seko, D.; Kitajima, Y.; Yoshioka, K.; Tsuchiya, Y.; Masuda, S.; Ono, Y. Notch1 and Notch2 coordinately regulate stem cell function in the quiescent and activated states of muscle satellite cells. *Stem Cells* **2018**, *36*, 278-285.
46. Mourikis, P.; Sambasivan, R.; Castel, D.; Rocheteau, P.; Bizzarro, V.; Tajbakhsh, S. A critical requirement for notch signaling in maintenance of the quiescent skeletal muscle stem cell state. *Stem cells* **2012**, *30*, 243-252.
47. Bröhl, D.; Vasyutina, E.; Czajkowski, M.T.; Griger, J.; Rassek, C.; Rahn, H.-P.; Purfürst, B.; Wende, H.; Birchmeier, C. Colonization of the satellite cell niche by skeletal muscle progenitor cells depends on Notch signals. *Developmental cell* **2012**, *23*, 469-481.
48. Schmidt, K.; Glaser, G.; Wernig, A.; Wegner, M.; Rosorius, O. Sox8 is a specific marker for muscle satellite cells and inhibits myogenesis. *Journal of Biological Chemistry* **2003**, *278*, 29769-29775.
49. Negro, S.; Lessi, F.; Duregotti, E.; Aretini, P.; La Ferla, M.; Franceschi, S.; Menicagli, M.; Bergamin, E.; Radice, E.; Thelen, M. CXCL 12α/SDF-1 from perisynaptic Schwann cells promotes regeneration of injured motor axon terminals. *EMBO molecular medicine* **2017**, *9*, 1000-1010.

50. Arnett, A.L.; Konieczny, P.; Ramos, J.N.; Hall, J.; Odom, G.; Yablonka-Reuveni, Z.; Chamberlain, J.R.; Chamberlain, J.S. Adeno-associated viral vectors do not efficiently target muscle satellite cells. *Molecular Therapy-Methods & Clinical Development* **2014**, *1*, 14038.
51. Ellis, B.L.; Hirsch, M.L.; Barker, J.C.; Connelly, J.P.; Steininger, R.J.; Porteus, M.H. A survey of ex vivo/in vitro transduction efficiency of mammalian primary cells and cell lines with Nine natural adeno-associated virus (AAV1-9) and one engineered adeno-associated virus serotype. *Virology journal* **2013**, *10*, 1-10.
52. Li, X.; Rydzewski, N.; Hider, A.; Zhang, X.; Yang, J.; Wang, W.; Gao, Q.; Cheng, X.; Xu, H. A molecular mechanism to regulate lysosome motility for lysosome positioning and tubulation. *Nature cell biology* **2016**, *18*, 404-417.
53. Fukunishi, A.; Maruyama, T.; Zhao, H.; Tiwari, M.; Kang, S.; Kumanogoh, A.; Yamamoto, N. The action of Semaphorin7A on thalamocortical axon branching. *Journal of neurochemistry* **2011**, *118*, 1008-1015.
54. Jeroen Pasterkamp, R.; Peschon, J.J.; Spriggs, M.K.; Kolodkin, A.L. Semaphorin 7A promotes axon outgrowth through integrins and MAPKs. *Nature* **2003**, *424*, 398-405.
55. Tang, F.; Kalil, K. Netrin-1 induces axon branching in developing cortical neurons by frequency-dependent calcium signaling pathways. *Journal of Neuroscience* **2005**, *25*, 6702-6715.
56. Dent, E.W.; Barnes, A.M.; Tang, F.; Kalil, K. Netrin-1 and semaphorin 3A promote or inhibit cortical axon branching, respectively, by reorganization of the cytoskeleton. *Journal of Neuroscience* **2004**, *24*, 3002-3012.
57. Hayano, Y.; Sasaki, K.; Ohmura, N.; Takemoto, M.; Maeda, Y.; Yamashita, T.; Hata, Y.; Kitada, K.; Yamamoto, N. Netrin-4 regulates thalamocortical axon branching in an activity-dependent fashion. *Proceedings of the National Academy of Sciences* **2014**, *111*, 15226-15231.
58. Dong, F.; Liu, Y.; Yan, W.; Meng, Q.; Song, X.; Cheng, B.; Yao, R. Netrin-4: Focus on Its Role in Axon Guidance, Tissue Stability, Angiogenesis and Tumors. *Cellular and Molecular Neurobiology* **2022**, 1-21.
59. McLoon, L.K.; Wirtschafter, J. Activated satellite cells are present in uninjured extraocular muscles of mature mice. *Transactions of the American Ophthalmological Society* **2002**, *100*, 119.
60. Ishimoto, S.; Goto, I.; Ohta, M.; Kuroiwa, Y. A quantitative study of the muscle satellite cells in various neuromuscular disorders. *Journal of the neurological sciences* **1983**, *62*, 303-314.
61. Scaramozza, A.; Marchese, V.; Papa, V.; Salaroli, R.; Soraru, G.; Angelini, C.; Cenacchi, G. Skeletal muscle satellite cells in amyotrophic lateral sclerosis. *Ultrastructural pathology* **2014**, *38*, 295-302.
62. Pradat, P.-F.; Barani, A.; Wanschitz, J.; Dubourg, O.; Lombès, A.; Bigot, A.; Mouly, V.; Bruneteau, G.; Salachas, F.; Lenglet, T. Abnormalities of satellite cells function in amyotrophic lateral sclerosis. *Amyotrophic Lateral Sclerosis* **2011**, *12*, 264-271.
63. Manzano, R.; Toivonen, J.M.; Calvo, A.C.; Oliván, S.; Zaragoza, P.; Rodellar, C.; Montarras, D.; Osta, R. Altered in vitro proliferation of mouse SOD1-G93A skeletal muscle satellite cells. *Neurodegenerative Diseases* **2013**, *11*, 153-164.
64. Manzano, R.; Toivonen, J.M.; Oliván, S.; Calvo, A.C.; Moreno-Igoa, M.; Muñoz, M.J.; Zaragoza, P.; García-Redondo, A.; Osta, R. Altered expression of myogenic regulatory factors in the mouse model of amyotrophic lateral sclerosis. *Neurodegenerative diseases* **2011**, *8*, 386-396.
65. Manzano, R.; Toivonen, J.M.; Calvo, A.C.; Oliván, S.; Zaragoza, P.; Muñoz, M.J.; Montarras, D.; Osta, R. Quantity and activation of myofiber-associated satellite cells in a mouse model of amyotrophic lateral sclerosis. *Stem Cell Reviews and Reports* **2012**, *8*, 279-287.
66. Lieberam, I.; Agalliu, D.; Nagasawa, T.; Ericson, J.; Jessell, T.M. A Cxcl12-CXCR4 chemokine signaling pathway defines the initial trajectory of mammalian motor axons. *Neuron* **2005**, *47*, 667-679.
67. Whitman, M.C.; Nguyen, E.H.; Bell, J.L.; Tenney, A.P.; Gelber, A.; Engle, E.C. Loss of CXCR4/CXCL12 signaling causes oculomotor nerve misrouting and development of motor trigeminal to oculomotor synkinesis. *Investigative ophthalmology & visual science* **2018**, *59*, 5201-5209.
68. Griffin, C.A.; Apponi, L.H.; Long, K.K.; Pavlath, G.K. Chemokine expression and control of muscle cell migration during myogenesis. *Journal of cell science* **2010**, *123*, 3052-3060.

69. Brzoska, E.; Kowalewska, M.; Markowska-Zagrajek, A.; Kowalski, K.; Archacka, K.; Zimowska, M.; Grabowska, I.; Czerwińska, A.M.; Czarnecka-Góra, M.; Stremińska, W. Sdf-1 (CXCL12) improves skeletal muscle regeneration via the mobilisation of Cxcr4 and CD34 expressing cells. *Biology of the Cell* **2012**, *104*, 722-737.
70. Donohoe, D.R.; Garge, N.; Zhang, X.; Sun, W.; O'Connell, T.M.; Bunger, M.K.; Bultman, S.J. The microbiome and butyrate regulate energy metabolism and autophagy in the mammalian colon. *Cell metabolism* **2011**, *13*, 517-526.
71. Guo, W.; Naujock, M.; Fumagalli, L.; Vandoorne, T.; Baatsen, P.; Boon, R.; Ordovás, L.; Patel, A.; Welters, M.; Vanwelden, T. HDAC6 inhibition reverses axonal transport defects in motor neurons derived from FUS-ALS patients. *Nature communications* **2017**, *8*, 861.
72. Paganoni, S.; Macklin, E.A.; Hendrix, S.; Berry, J.D.; Elliott, M.A.; Maiser, S.; Karam, C.; Caress, J.B.; Owegi, M.A.; Quick, A. Trial of sodium phenylbutyrate–taurursodiol for amyotrophic lateral sclerosis. *New England Journal of Medicine* **2020**, *383*, 919-930.
73. Gurney, M.E.; Pu, H.; Chiu, A.Y.; Dal Canto, M.C.; Polchow, C.Y.; Alexander, D.D.; Caliendo, J.; Hentati, A.; Kwon, Y.W.; Deng, H.-X. Motor neuron degeneration in mice that express a human Cu, Zn superoxide dismutase mutation. *Science* **1994**, *264*, 1772-1775.
74. Luo, G.; Yi, J.; Ma, C.; Xiao, Y.; Yi, F.; Yu, T.; Zhou, J. Defective mitochondrial dynamics is an early event in skeletal muscle of an amyotrophic lateral sclerosis mouse model. *PloS one* **2013**, *8*, e82112.
75. Mizuguchi, H.; Xu, Z.; Ishii-Watabe, A.; Uchida, E.; Hayakawa, T. IRES-dependent second gene expression is significantly lower than cap-dependent first gene expression in a bicistronic vector. *Molecular Therapy* **2000**, *1*, 376-382.